geosciences

MDPI

Article

A Multi-proxy Provenance Study of Late Carboniferous to Middle Jurassic Sandstones in the Eastern Sverdrup Basin and Its Bearing on Arctic Palaeogeographic Reconstructions

Michael A. Pointon [1,*], Helen Smyth [1,2], Jenny E. Omma [1,3], Andrew C. Morton [1,4,*], Simon Schneider [1], Peter Hülse [1,5], Stephen J. Rippington [1,6], Berta Lopez-Mir [1,7], Quentin G. Crowley [8], Ian Millar [9], Martin J. Whitehouse [10], Dirk Frei [11], Robert A. Scott [1,†] and Michael J. Flowerdew [1]

1 CASP, West Building, Madingley Rise, Madingley Road, Cambridge CB3 0UD, UK
2 Halliburton, 97 Jubilee Avenue, Milton Park, Abingdon OX14 4RW, UK
3 Rocktype Ltd., Magdalen Centre, Robert Robinson Avenue, Oxford OX4 1LN, UK
4 Department of Geology and Geophysics, University of Aberdeen, Aberdeen AB24 3UE, UK
5 LechRocks, Am Geräumtweg 2, 86899 Landsberg am Lech, Germany
6 Astute Geoscience Ltd., 49 Station Road, Polegate, East Sussex BN26 6EA, UK
7 Departamento de Biología y Geología, Física y Química Inorgánica, Universidad Rey Juan Carlos, Campus de Móstoles, Calle Tulipán, Móstoles, 28933 Madrid, Spain
8 Department of Geology, School of Natural Sciences, Trinity College Dublin, College Green, D02 PN40 Dublin, Ireland
9 Geochronology and Tracers Facility, British Geological Survey, Keyworth NG12 5GG, UK
10 Department of Geosciences, Swedish Museum of Natural History, SE-104 05 Stockholm, Sweden
11 Department of Earth Sciences, University of the Western Cape, Private Bag X17, Bellville 7530, South Africa
* Correspondence: michael.pointon@casp.org.uk (M.A.P.); heavyminerals@hotmail.co.uk (A.C.M.)
† Deceased.

check for updates

Citation: Pointon, M.A.; Smyth, H.; Omma, J.E.; Morton, A.C.; Schneider, S.; Hülse, P.; Rippington, S.J.; Lopez-Mir, B.; Crowley, Q.G.; Millar, I.; et al. A Multi-proxy Provenance Study of Late Carboniferous to Middle Jurassic Sandstones in the Eastern Sverdrup Basin and Its Bearing on Arctic Palaeogeographic Reconstructions. *Geosciences* **2023**, *13*, 10. https://doi.org/10.3390/geosciences13010010

Academic Editors: Jesus Martinez-Frias and Angelos G. Maravelis

Received: 26 October 2022
Revised: 15 December 2022
Accepted: 20 December 2022
Published: 28 December 2022

Abstract: A multi-proxy provenance study of Late Carboniferous to Middle Jurassic sandstones from the eastern Sverdrup Basin was undertaken employing optical petrography and heavy mineral analysis, chemical analysis of apatite, garnet and rutile grains, as well as detrital zircon U–Pb geochronology and Hf isotope analysis. Late Carboniferous to Middle Jurassic strata on the southern basin margin are inferred as being predominantly reworked from Silurian to Devonian strata within the adjacent Franklinian Basin succession. Higher-grade metamorphic detritus appeared during Middle to Late Triassic times and indicates exhumation and erosion of lower (Neoproterozoic to Cambrian) levels within the Franklinian Basin succession and/or a direct detrital input from the Canadian-Greenland Shield. The provenance of northern-derived sediments is more enigmatic owing to the subsequent opening of the Arctic Ocean. Northern-derived Middle Permian to Early Triassic sediments were likely derived from proximal areas of the Chukotkan part of the Arctic Alaska-Chukotka microplate. Late Triassic northern-derived sediments have different detrital zircon U–Pb age spectra from Middle Permian to Early Triassic ones and were likely derived from the Uralian orogenic belt and/or the Arctic Uralides. The loss of this sand input during latest Triassic times is interpreted to reflect drainage reorganisation farther upstream on the Barents Shelf. Middle Jurassic sands in the northern and axial parts of the basin were largely reworked from local northern-derived Late Triassic strata. This may have been facilitated by rift flank uplift of the northern basin margin in response to rifting in the adjacent proto-Amerasia Basin.

Keywords: detrital zircon; U-Pb geochronology; Lu-Hf isotopes; mineral chemistry; heavy mineral analysis; Amerasia Basin

1. Introduction

How and when the Amerasia Basin (Figure 1a) opened are issues that have vexed scientists for decades [1–6]. This is in part due to the paucity of direct evidence and

subsequent overprinting by volcanism centred on the Alpha-Mendeleev Ridge (Figure 1a). The basin is generally considered to have opened during Jurassic to Early Cretaceous times (*c*. 195–127.5 Ma according to [3]), although a later opening, after Aptian-Albian times (*c*. 100.5–125 Ma), has also been proposed [7]. Sedimentary basins exposed along the Arctic continental margins provide a valuable record of the tectonic setting and crustal affinity of nearby terranes, and can provide insight into the pre-rift configuration of Arctic terranes. This has been demonstrated by countless sediment provenance studies from the Arctic region (e.g., [8–15], to name a few). Despite these efforts, considerable uncertainties remain regarding how some of the now disparate Arctic margins once fitted together and how sediment was routed between them. The purpose of this study is to constrain the provenance of Late Carboniferous to Middle Jurassic sands of the eastern Sverdrup Basin, and thereby help to identify sediment routing pathways and terranes that lay to the north of the basin.

The Sverdrup Basin (Figure 1a–c) provides a near-continuous record of Carboniferous to Cretaceous strata, spanning the pre-rift to post-drift interval. During the Carboniferous to Middle Jurassic interval, siliciclastic sediment was supplied into the basin from two main directions: the south/east and the north/northeast (e.g., [16–19]; all directions given are present-day coordinates). These directions are well established from thickness and facies information, as well as palaeocurrent data. Sediment supplied from the south and east is inferred as being derived from the adjacent Franklinian Basin succession and/or the Canadian-Greenland Shield [18–20]. This is supported by limited U–Pb zircon data [10,21] and whole-rock Sm–Nd isotopic data [22]. The relative detrital contributions from these areas, and how they vary through time, are poorly constrained, however.

During Middle Permian to Middle Jurassic times, sediment also intermittently entered the basin from the north (e.g. [15,18–20]). The provenance of these sands is both cryptic and contentious owing to the source area being dissected from the basin during the subsequent opening of the Amerasia Basin. These sands have been suggested to have originated from an enigmatic landmass, termed Crockerland (e.g., [17,23]) or Arctida (e.g., [24,25]), which lay proximal to the northern basin margin [17,23]. According to the most widely accepted model for the opening of the Amerasia Basin (rotational/windscreen wiper model [3,26–28]) the Arctic Alaska-Chukotka microplate (AACM; Figure 1a) restores against the Canadian Arctic margin [7]. Part of this microplate formed Crockerland [29]. Recent provenance studies, based largely on detrital zircon U–Pb age data, have provided additional insights into the provenance of the northern-derived sands and Crockerland. Middle Permian to Early Triassic sands on northern Axel Heiberg Island contain abundant Permian zircons, which led Alonso-Torres et al. [15] and Hadlari et al. [30] to suggest that Crockerland formed part of a magmatic arc system. This was, however, contested by Galloway et al. [31] as similar-aged sands farther to the southwest in the basin lack Permian zircons [31,32]. Late Triassic strata from the Pat Bay Formation and the Romulus Member of the Heiberg Formation contain numerous Carboniferous to Triassic detrital zircons, which have been interpreted as being derived from a northern magmatic arc [30,33] and conversely the Uralian orogen [32,34] and its inferred Arctic extension incorporating the Pai-Khoi Range, Novaya Zemlya and Taimyr (Arctic Uralides; e.g., [35]). Understanding the source(s) of these sands, and constraining when they appear and disappear from the Sverdrup Basin record has implications for regional palaeogeographic reconstructions. For example, Early Jurassic strata have been shown to lack near syn-depositional aged detrital zircons unlike Late Triassic sands [33]. This has been inferred to reinforce earlier suggestions that rifting in the proto-Amerasia Basin led to the dissection of the northern source area [17–19,23,29,33,36].

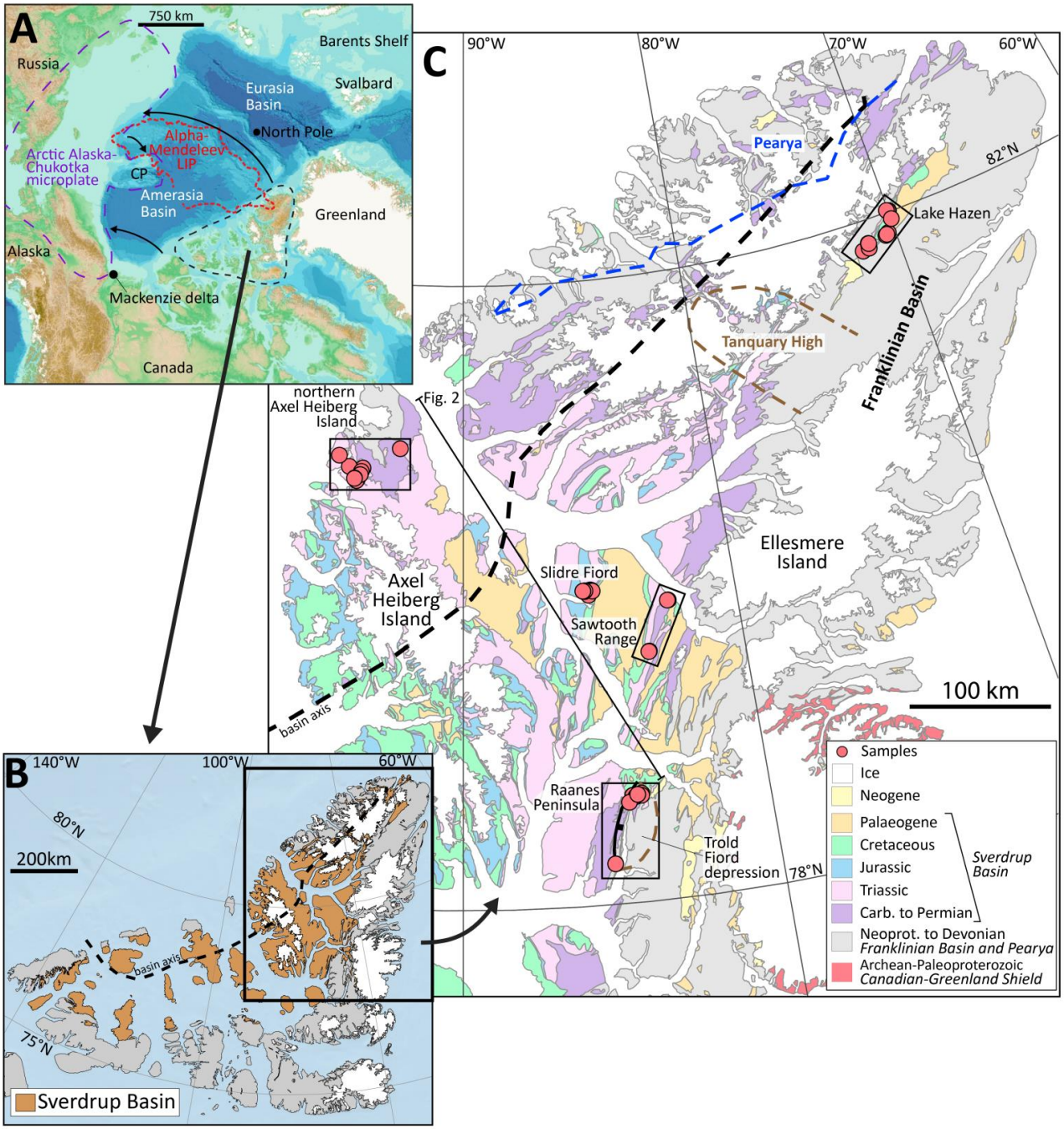

Figure 1. Maps of the Arctic region and Sverdrup Basin showing the locations of samples analysed in this study. (**A**) map of the Arctic region (from [37]). The black arrows summarise the rotation/windscreen wiper model for the opening of the Arctic Ocean [3], with anticlockwise rotation about a pole centred approximately over the Mackenzie Delta and subsequent clockwise rotation of the Chukchi Plateau (CP). The outline of the Alpha-Mendeleev large igneous province (LIP) is from Pease et al. [6] and the outline of the Arctic Alaska-Chukotka microplate is from Miller et al. [7]. (**B**,**C**) Geological maps of the Sverdrup Basin (simplified from [38]). The basin axis is redrawn from Embry and Beauchamp [18,19]. The approximate line of section drawn in Figure 2 is indicated in (**C**). Carb = Carboniferous; Neoprot = Neoproterozoic.

Whilst detrital zircon U–Pb age data can provide insights, the high physical and chemical stability of zircon means that it is prone to surviving multiple sedimentary cycles, which can obfuscate provenance interpretations. Consequently, the aim of this study is

to provide a better understanding of the provenance of Late Carboniferous to Middle Jurassic siliciclastic sediments within the eastern Sverdrup Basin through a multi-analytical approach. Samples were analysed from the northern and southern flanks of the basin using a combination of optical petrography, conventional heavy mineral analysis, chemical analysis of apatite, garnet and rutile grains, and combined detrital zircon U–Pb age and Hf isotope analysis. These data are integrated with published data to better characterise sediment inputs into the basin through time.

2. Geological Background

The study area comprises four main geological elements: the Canadian-Greenland Shield, the Franklinian Basin, Pearya and the Sverdrup Basin (Figure 1c). The oldest rocks in the area are Archean to Paleoproterozoic highly deformed, granulite facies, metasedimentary and metaigneous rocks of the Canadian-Greenland Shield [16,39–41]. These are exposed on southeast Ellesmere Island (Figure 1c). The Franklinian Basin succession is a package of late Neoproterozoic to Late Devonian sedimentary rocks more than 8 km thick, which was deposited on the northern margin of Laurentia (Figure 1c; [42–46]). Between late Neoproterozoic and Ordovician times, mixed siliciclastic and carbonate sediments were deposited in shelf to basinal environments in a passive margin setting [31,42,46–48]. Clastic strata within these units are inferred as being derived primarily from the Canadian-Greenland Shield [42,47,49].

Pearya is a composite terrane exposed on northern Ellesmere Island (Figure 1c; e.g., [50–52]). Its origin is controversial and beyond the scope of this study, although it is inferred to have been in its present location by Llandovery to Ludlow times based on overlapping stratal relationships [53]. Pearya comprises crystalline basement including latest Mesoproterozoic to earliest Neoproterozoic granitoids and gneisses overlain by Neoproterozoic metasedimentary rocks and an Ordovician to Silurian arc-related sedimentary and volcanic succession [51,52,54–57].

During Silurian times, the Franklinian Basin received substantial volumes of turbidites, interpreted as flysch, sourced from the east, from the Greenland and Svalbard Caledonides, and Pearya [42,49,58]. By Middle Devonian times, the Franklinian Basin had transitioned into a foreland basin and was accumulating fluvial and deltaic sediments. These are often referred to as the Devonian clastic wedge (e.g., [44,45,59–61]). The origin of the foreland basin has been linked to mid-Devonian collisional events that culminated in the Late Devonian to Mississippian Ellesmerian Orogeny [42,43]. The orogeny may have resulted from the collision of Crockerland with the northern Laurentian margin [23,29,42,43]. Sediments of the Devonian clastic wedge are inferred as being initially derived chiefly from the East Greenland Caledonides, Pearya and the Ellesmerian orogenic belt, with the last area eventually dominating sediment supply [42,43,61]. Orogenic collapse and rifting occurred during Early Carboniferous times, after which sedimentation commenced within the successor Sverdrup Basin (e.g., [18,19]).

Sverdrup Basin

The Sverdrup Basin covers an area of ~300,000 km^2 and has been estimated to contain up to 13–15 km thickness of Carboniferous to Eocene sedimentary strata (Figure 1a–c; [16,18,19]). Active rifting occurred between Viséan and Bashkirian times, after which the basin experienced a more complex transpressional/transtensional stress regime until Early Permian times [18,19,62]. Initial sedimentation within the basin was fluvial to marginally marine and occurred within actively rifting sub-basins that became progressively more interconnected (Emma Fiord to lower Canyon Fiord formations in Figure 2; [18]). Mafic volcanic rocks of the lowermost part of the Borup Fiord Formation and Audhild volcanics were erupted onto northern Ellesmere and Axel Heiberg islands during this time [63,64]. Sedimentation during much of the remaining Late Carboniferous to Early Permian interval was characterised by the deposition of mixed carbonate and siliciclastic sediments (Figure 2). During Bashkirian times, waters within the basin became intermittently hypersaline leading to

the deposition of evaporite beds in the axial parts of the basin [65]. These are intercalated with limestones, shales and sandstones, which collectively form the Otto Fiord Formation (Figure 2; [18,65]). Sporadic mafic volcanism occurred on northern Ellesmere and Axel Heiberg islands during Sakmarian to Artinskian and Kungurian times (unnamed lower volcanics and Esayoo Formation, respectively; Figure 2; [66,67]).

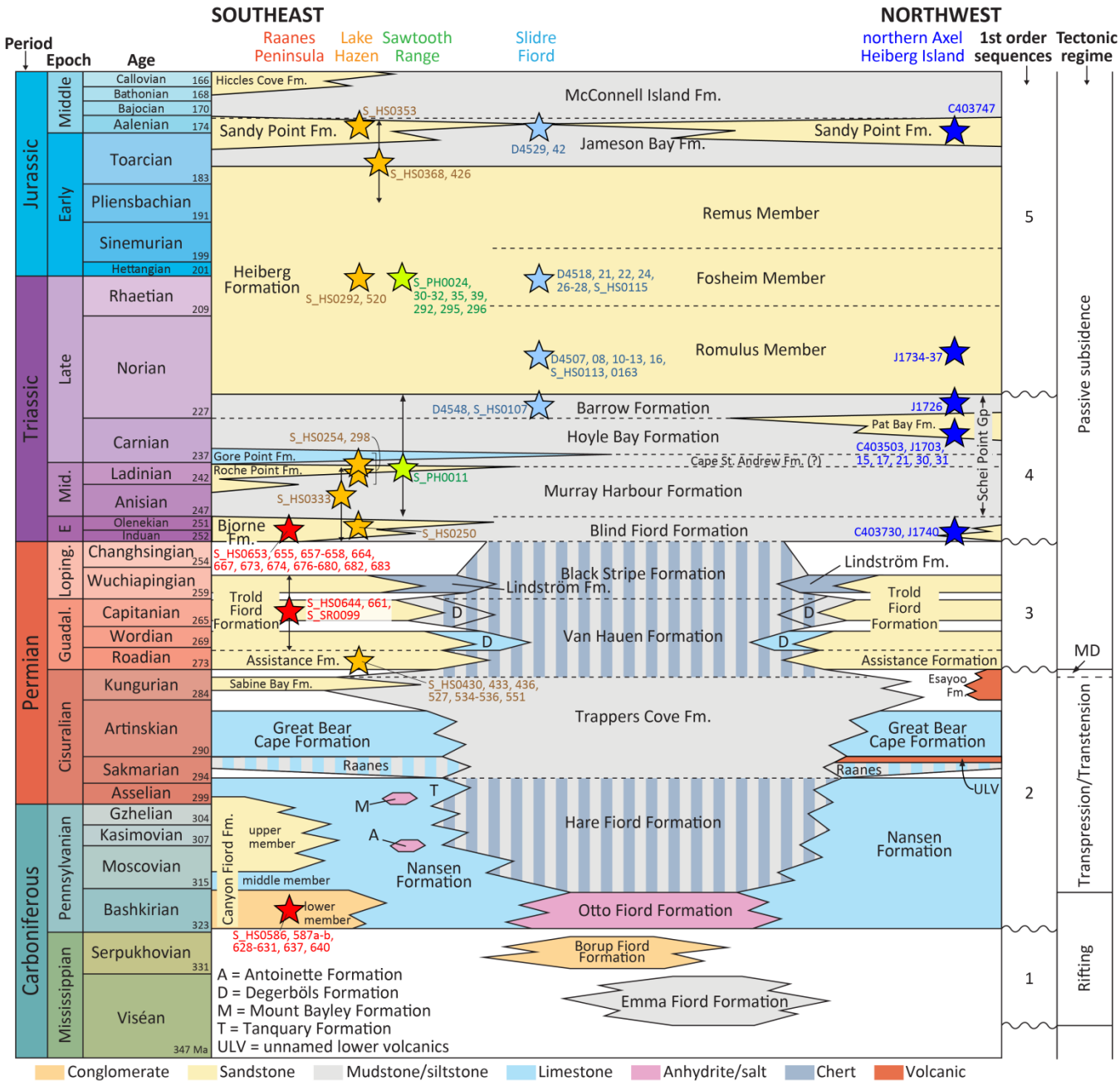

Figure 2. Carboniferous to Middle Jurassic lithostratigraphic framework of the eastern Sverdrup Basin showing the sampled units. The stars represent samples. The figure is adapted from Lopez-Mir et al. [68] using information in Davies and Nassichuk [63], Embry [17,20,23,69] and Embry and Beauchamp [18,19]. Numerical ages are from Cohen et al. [70]. First-order sequences and tectonic regime are from Embry and Beauchamp [18]. MD = Melvillian Disturbance.

An angular unconformity separates pre-Roadian from younger strata, and is attributed to compression/basin inversion linked to the Melvillian Disturbance (Figure 2; [15,62,71]). Following this, sandstones were deposited on both the northern and southern basin margins

(Assistance and Trold Fiord formations; Figure 2), which mark the first substantial sand input into the Sverdrup Basin from the north [15,31]. Thickness and facies data suggest that sediment supply from the north into the eastern Sverdrup Basin waned during Early Triassic times [17].

From Middle Permian until Early Cretaceous times the basin is traditionally viewed as an intracratonic basin dominated by passive thermal subsidence [18–20,72,73]. Salt tectonics were active during this time, however, with salt diapirs sourced from the Otto Fiord Formation rising since at least the start of the Triassic Period [68,74,75]. The basin experienced high rates of subsidence during Early Triassic times, resulting in a large bathymetric difference of probably more than 2 km between the basin margins and basin axis [18]. This, together with the occurrence of Triassic volcanic ash layers on northern Axel Heiberg Island, has led to suggestions that the basin may have occupied a retro-arc foreland setting during at least the Middle Permian to Triassic interval [15,30,33]. Alternative origins for the Early Triassic volcanic ash layers include sources from the Siberian Traps (*cf.* [76,77]) and indicate the causes for rapid subsidence and volcanism may not be related.

Throughout Triassic to Middle Jurassic times, sedimentation within the basin was almost exclusively siliciclastic. The basin centre was mud-dominated (Blind Fiord to McConnell Island formations; Figure 2) whilst a series of deltaic or marine shelfal sands prograded into the basin from the margins (Bjorne Formation through to Hiccles Cove Formation; sandstone-dominated formations in Figure 2). The Late Triassic interval was marked by renewed, substantial sand input from the north of the basin (Pat Bay Formation and Romulus Member of the Heiberg Formation; Figure 2). It has been suggested that over 100,000 km^3 of northern-derived sediment were deposited in the Sverdrup Basin during Norian times [18]. As a consequence, sediment supply outstripped subsidence and by the end of the Norian Age the central deep-water part of the basin was filled [16,18–20]. The northern source area is inferred to have been cut off from the basin during Jurassic times [17–19,29,30,33]. The source for the northern-derived sediment is controversial, with models existing for a Crockerland source [17,23,30,33] and for progradation of fluvio-deltaic systems across the Barents Shelf that originated from the Uralian Orogen and its Arctic Uralides extension [32,34,78]. Subsidence analysis suggests that the basin experienced extension from Oxfordian until Early Cretaceous times [72]. Cross-section balancing analysis suggests that fault activity may have also occurred during Triassic times [68]. Apart from several volcanic ash beds that occur interbedded with Triassic strata on northwest Axel Heiberg Island [30,33], Triassic to Jurassic volcanism is not known from the basin.

3. Materials and Methods

3.1. Samples

Ninety samples have been analysed as part of this study. They were collected from five main areas within the basin, which are: (1) northern Axel Heiberg Island; (2) the Lake Hazen area; (3) Slidre Fiord; (4) the Sawtooth Range; and (5) the Raanes Peninsula (Figure 1c; Table 1). Samples from northern Axel Heiberg Island are from the northern flank of the basin; all other samples are from the inferred axial region of the basin or its southern flank (Figures 1 and 2). Most of the samples were collected during several field seasons between 2007 and 2013. This is apart from samples with C40 prefixes, which were provided by Ashton Embry.

In detail, nine samples were investigated from the Bashkirian lower Canyon Fiord Formation on the Raanes Peninsula (Table 1; Figure 2). In this area, the formation comprises alluvial and fluvial strata (red breccias and coarse sandstones) that were deposited in a series of NNE-SSW-orientated half grabens [79]. The samples analysed were collected from the Trold Fiord depression (Figure 1c; [79]). Eight sandstone samples were investigated from the Roadian Assistance Formation, which were collected from outcrop sections along the north shore of Lake Hazen (Table 1; Figure 2). In this area, the Assistance Formation comprises mixed carbonate and siliciclastic sediments inferred as being deposited in fluvial/flood plain to proximal marine shelf environments. Three sandstone samples were taken from the

Wordian to Wuchiapingian Trold Fiord Formation (Table 1), from outcrops on the Raanes Peninsula area, where the formation comprises green, glauconitic, calcareous sandstones and sandy limestones interpreted as being deposited under shallow marine conditions with limited siliciclastic input.

Table 1. A list of the samples studied and the analyses undertaken. All samples are sandstones apart from D4548, J1703, J1740, S_HS0292 and S_HS0631 (siltstones), as well as S_HS0250 and S_HS0640 (limestones). Further lithological information and sampling co-ordinates are provided in the supplementary materials (Table S1). * Data were presented by Omma et al. [34].

Sample Number	Region	Formation	Member	Petrography	Heavy Mineral Analysis	Geochemistry			Zircon U–Pb	Zircon Lu–Hf
						Apatite	Garnet	Rutile		
D4542	Slidre Fiord	Sandy Point		Y	Y				Y	Y
D4529	Slidre Fiord	Sandy Point		Y						
C403747	N. Axel Heiberg Island	Sandy Point		Y	*				*	Y
S_HS0426	Lake Hazen	Sandy Point		Y						
S_HS0368	Lake Hazen	Sandy Point or Heiberg		Y	Y					
S_HS0353	Lake Hazen	Sandy Point or Heiberg		Y	Y			Y	Y	
S_HS0520	Lake Hazen	Heiberg(?)		Y	Y			Y		
S_HS0292	Lake Hazen	Heiberg(?)			Y					
S_PH0296	Sawtooth Range	Heiberg			Y			Y		
S_PH0295	Sawtooth Range	Heiberg			Y			Y		
S_PH0292	Sawtooth Range	Heiberg			Y			Y	Y	
S_PH0039	Sawtooth Range	Heiberg			Y			Y		
S_PH0035	Sawtooth Range	Heiberg			Y					
S_PH0032	Sawtooth Range	Heiberg			Y					
S_PH0031	Sawtooth Range	Heiberg			Y					
S_PH0030	Sawtooth Range	Heiberg			Y			Y	Y	
S_PH0024	Sawtooth Range	Heiberg			Y					
S_HS0115	Slidre Fiord	Heiberg	Fosheim		Y					
D4528	Slidre Fiord	Heiberg	Fosheim	Y	Y			Y	Y	
D4527	Slidre Fiord	Heiberg	Fosheim	Y	Y					
D4526	Slidre Fiord	Heiberg	Fosheim	Y						
D4524	Slidre Fiord	Heiberg	Fosheim	Y	Y					
D4522	Slidre Fiord	Heiberg	Fosheim	Y	Y			Y		
D4521	Slidre Fiord	Heiberg	Fosheim	Y	Y				Y	
D4518	Slidre Fiord	Heiberg	Fosheim	Y	Y					
S_HS0163	Slidre Fiord	Heiberg	Romulus		Y	Y		Y		
S_HS0113	Slidre Fiord	Heiberg	Romulus		Y					
D4516	Slidre Fiord	Heiberg	Romulus	Y	Y	Y		Y		
D4513	Slidre Fiord	Heiberg	Romulus	Y	Y					
D4512	Slidre Fiord	Heiberg	Romulus	Y	Y	Y	Y	Y	Y	
D4511	Slidre Fiord	Heiberg	Romulus	Y	Y					
D4510	Slidre Fiord	Heiberg	Romulus	Y						
D4508	Slidre Fiord	Heiberg	Romulus		Y				Y	
D4507	Slidre Fiord	Heiberg	Romulus	Y						
J1737	N. Axel Heiberg Island	Heiberg	Romulus	Y	Y				Y	Y
J1736	N. Axel Heiberg Island	Heiberg	Romulus	Y	Y					
J1735	N. Axel Heiberg Island	Heiberg	Romulus	Y						
J1734	N. Axel Heiberg Island	Heiberg	Romulus	Y						
S_PH0011	Sawtooth Range	(Schei Point Group, undifferentiated)			Y					
S_HS0107	Slidre Fiord	Barrow			Y	Y				
D4548	Slidre Fiord	Barrow			Y					
J1726	N. Axel Heiberg Island	Barrow		Y	Y					
J1731	N. Axel Heiberg Island	Pat Bay/Hoyle Bay		Y						
J1730	N. Axel Heiberg Island	Pat Bay/Hoyle Bay		Y						
J1721	N. Axel Heiberg Island	Pat Bay/Hoyle Bay		Y	Y					
J1717	N. Axel Heiberg Island	Pat Bay/Hoyle Bay		Y	Y				Y	Y
J1715	N. Axel Heiberg Island	Pat Bay/Hoyle Bay		Y	Y					

Table 1. *Cont.*

Sample Number	Region	Formation	Member	Petrography	Heavy Mineral Analysis	Geochemistry			Zircon U–Pb	Zircon Lu–Hf
						Apatite	Garnet	Rutile		
J1703	N. Axel Heiberg Island	Pat Bay/Hoyle Bay		Y	Y					
C403503	N. Axel Heiberg Island	Pat Bay/Hoyle Bay		Y	*				*	Y
S_HS0298	Lake Hazen	Roche Point or Gore Point		Y	Y	Y				
S_HS0254	Lake Hazen	Roche Point or Gore Point		Y	Y	Y		Y	Y	
S_HS0333	Lake Hazen	Bjorne or Roche Point		Y	Y	Y		Y		
J1740	N. Axel Heiberg Island	Blind Fiord		Y						
C403730	N. Axel Heiberg Island	Blind Fiord		Y	*				*/Y	Y
S_HS0250	Lake Hazen	Bjorne(?)		Y						
S_HS0683	Raanes Peninsula	Bjorne			Y					
S_HS0682	Raanes Peninsula	Bjorne		Y	Y					
S_HS0680	Raanes Peninsula	Bjorne		Y	Y					
S_HS0679	Raanes Peninsula	Bjorne			Y					
S_HS0678	Raanes Peninsula	Bjorne		Y	Y					
S_HS0677	Raanes Peninsula	Bjorne		Y						
S_HS0676	Raanes Peninsula	Bjorne		Y	Y					
S_HS0674	Raanes Peninsula	Bjorne		Y	Y	Y	Y	Y		
S_HS0673	Raanes Peninsula	Bjorne		Y	Y	Y	Y			
S_HS0667	Raanes Peninsula	Bjorne		Y	Y					
S_HS0664	Raanes Peninsula	Bjorne		Y	Y					
S_HS0658	Raanes Peninsula	Bjorne		Y	Y	Y		Y	Y	
S_HS0657	Raanes Peninsula	Bjorne		Y	Y	Y				
S_HS0655	Raanes Peninsula	Bjorne		Y	Y					
S_HS0653	Raanes Peninsula	Bjorne		Y	Y	Y		Y	Y	
S_SR0099	Raanes Peninsula	Trold Fiord			Y					
S_HS0661	Raanes Peninsula	Trold Fiord		Y	Y			Y	Y	
S_HS0644	Raanes Peninsula	Trold Fiord		Y	Y			Y		
S_HS0551	Lake Hazen	Assistance			Y			Y	Y	
S_HS0536	Lake Hazen	Assistance		Y	Y					
S_HS0535	Lake Hazen	Assistance		Y						
S_HS0534	Lake Hazen	Assistance		Y	Y			Y		
S_HS0527	Lake Hazen	Assistance		Y	Y			Y	Y	
S_HS0436	Lake Hazen	Assistance		Y						
S_HS0433	Lake Hazen	Assistance		Y	Y			Y		
S_HS0430	Lake Hazen	Assistance		Y						
S_HS0640	Raanes Peninsula	Canyon Fiord			Y					
S_HS0637	Raanes Peninsula	Canyon Fiord		Y	Y	Y	Y	Y		
S_HS0631	Raanes Peninsula	Canyon Fiord		Y	Y	Y				
S_HS0630	Raanes Peninsula	Canyon Fiord		Y	Y			Y	Y	
S_HS0629	Raanes Peninsula	Canyon Fiord		Y	Y			Y	Y	
S_HS0628	Raanes Peninsula	Canyon Fiord		Y	Y					
S_HS0587b	Raanes Peninsula	Canyon Fiord		Y						
S_HS0587a	Raanes Peninsula	Canyon Fiord		Y						
S_HS0586	Raanes Peninsula	Canyon Fiord		Y	Y			Y	Y	

Fifteen samples of deltaic sandstones were investigated from the Early Triassic Bjorne Formation from outcrops on the Raanes Peninsula (Table 1; Figure 2). The Bjorne Formation consists mainly of delta plain and fluvial facies [80–82]. Two samples are from the mudstone-dominated Blind Fiord Formation on northern Axel Heiberg Island (Table 1; Figure 2). The formation here is interpreted to record a slope to basin floor depositional environment [81].

On northern Axel Heiberg Island slope to basinal mudstones of the Carnian Hoyle Bay Formation are interpreted to be partially intercalated with and partially overlain by nearshore-shallow marine and basinal sandstones of the late Carnian Pat Bay Formation [20,83]. Seven samples are from this interval (Table 1; Figure 2). As these formations are interbedded in this area, the samples are described as being from the Pat Bay/Hoyle Bay Formation in subsequent sections. Three samples of the Norian Barrow Formation were

collected from outcrops on northern Axel Heiberg Island and near Slidre Fiord (Table 1; Figure 2). The formation is dominated by shales and siltstones with minor very fine-grained sandstones interpreted as prodelta to offshore marine shelf/slope deposits [20,83]. Conventional heavy mineral data were also obtained from a sandstone of the Anisian to Norian Schei Point Group in the Sawtooth Range (S_PH0011; Figure 2).

Thirty samples were analysed from the Norian to Pliensbachian or early Toarcian Heiberg Formation (Table 1; [84]). Thirteen are from the Romulus Member on northern Axel Heiberg Island and at Slidre Fiord (Table 1; Figure 2). The member comprises predominantly very fine to fine-grained delta-front sandstones [20,85,86]. Eight samples were analysed from the overlying Fosheim Member at Slidre Fiord (Table 1; Figure 2). This member comprises mainly fine- to medium-grained sandstones deposited in a delta plain environment [20,85,86]. Nine further samples were analysed from the Heiberg Formation in the Sawtooth Range (Table 1; Figure 2). Here, the member boundaries were not clear and so these samples are labelled as undifferentiated Heiberg Formation.

Six Triassic samples collected from outcrops to the north of Lake Hazen have less precise stratigraphic ages. Based on limited macrofossil and palynology data, and lithostratigraphic comparisons, sample S_HS0250 is probably from the Bjorne Formation, sample S_HS0333 is likely from the Bjorne or Roche Point formations, samples S_HS0254 and S_HS0298 are likely from the Roche Point or Gore Point formations, and samples S_HS0292 and S_HS0520 are probably from the Heiberg Formation (Figure 2). Two further samples from the same area are of late Pliensbachian to Aalenian age, and are from the Heiberg or Sandy Point formations (S_HS0353 and S_HS0368).

Four samples were investigated from the late Toarcian to Aalenian Sandy Point Formation. These were collected from the Lake Hazen area, northern Axel Heiberg Island and Slidre Fiord (Table 1; Figure 2). The Sandy Point Formation overlies the Jameson Bay Formation and consists of coarsening-upward cycles of shale, siltstone and sandstone [20,69]. The sandstone strata are interpreted as being deposited on a shallow marine shelf, mostly below wave base [20].

3.2. Methods

The samples were investigated using a multi-analytical approach commencing with optical petrography analysis and/or conventional heavy mineral analysis, followed by single grain chemical analysis (apatite, garnet and rutile) and detrital zircon U–Pb geochronology. Northern-derived samples were also subject to detrital zircon Lu–Hf isotope analysis. A breakdown of the analyses undertaken on each sample is given in Table 1. Summaries of the methods employed are given in subsequent sections; further methodology details are provided in the supplementary materials (Supplementary File S1) along with the analytical data tables (Supplementary Tables S1–S8).

3.2.1. Petrography

Thin sections were stained for porosity and alkali feldspar, and then point counted using a binocular microscope equipped with a digital point counting stage. Samples from northern Axel Heiberg Island and Slidre Fiord were counted using the Gazzi-Dickinson method [87], whereas samples from the Lake Hazen area and the Raanes Peninsula were counted using the Traditional/Indiana method [88]. The main difference between the Gazzi-Dickinson and Traditional/Indiana methods is in the classification of coarse-grained polymineralic grains. Such grains are, however, relatively rare within the dataset, minimising the difference between the two datasets. Sandstones were classified using the scheme of Pettijohn et al. [89].

3.2.2. Conventional Heavy Mineral Analysis

Heavy minerals were separated from the 63–125 μm grain size fraction, mounted in Canada Balsam and counted using a polarising microscope. Heavy mineral proportions were estimated based on 200 counts of non-opaque grains using the ribbon method

described by Galehouse [90]. The provenance-sensitive heavy mineral indices ATi (apatite:tourmaline index), GZi (garnet:zircon index), RuZi (rutile:zircon index), MZi (monazite:zircon index) and CZi (chrome spinel:zircon index) were determined following Morton and Hallsworth [91]. These were also determined using the ribbon counting method, ideally on the basis of a 200 grain count, although this was not always possible owing to low heavy mineral yields. The heavy mineral assemblage from sample S_HS0676 was swamped by carbonate minerals necessitating a hydrochloric acid treatment before counting. This treatment also dissolved apatite meaning apatite counts and the ATi values were not determined. Data from samples C403730, C403503 and C403747 are from Omma et al. [34].

3.2.3. Mineral Chemistry

The trace element chemistry of apatite and rutile grains was determined by laser ablation inductively coupled plasma mass spectrometry (LA-ICPMS) at Cardiff University. Apatite grains were assigned possible source lithology groups based on their Sr/Y ratios and light rare earth element (LREE) concentrations following the classification scheme of O'Sullivan et al. [92]. Rutile grains were classified into metapelitic and metamafic types based on Cr and Nb concentrations following Meinhold et al. [93]. Rutile metamorphic temperatures were estimated using the Zr-in-rutile thermometer calibration of Watson et al. [94]. The major element chemistry of garnet grains was determined by electron microprobe analysis at the British Geological Survey, the University of Aberdeen and the University of Cambridge. Garnet grains were assigned possible host rock types and metamorphic facies following Schönig et al. [95].

3.2.4. Detrital Zircon U–Pb Geochronology

Zircons were concentrated from the heavy mineral separates through heavy liquid separation with methylene iodide and magnetic separation. Detrital zircons were analysed at University College London (UK), Laurentian University (Ontario, Canada) and Stellenbosch University (South Africa) using LA-ICPMS, and at the NORDSIM facility (Swedish Natural History Museum, Stockholm, Sweden) using secondary ion mass spectrometry (SIMS) analysis. All of the analyses are single spot analyses. Concordia ages (*sensu* [96]) are used to avoid arbitrary switching between U–Pb age systems and were calculated using Isoplot v.4 [97]. Imprecise analyses (i.e., those with concordia age uncertainties >10%, 2s) and analyses >10% discordant (calculated at the limit of the 95% confidence uncertainty ellipse) are excluded from the interpretation. Probability density plots were drawn in R using the Detzrcr package [98].

3.2.5. Detrital Zircon Hafnium Isotope Analysis

Zircon grains were analysed for Lu–Hf isotopic ratios at the Geochronology and Tracers Facility, British Geological Survey, UK, using the LA-ICPMS method. The methodology closely followed that of Thomas et al. [99]. A 35 µm laser spot size was used, with spot analyses located on top of previous U–Pb SIMS analyses. Hf analyses from samples C403503 (Pat Bay Formation), C403747 (Sandy Point Formation), and 44 analyses from sample C403730 (Blind Fiord Formation) were undertaken over U–Pb spot analyses performed and reported by Omma et al. [34]. All other Hf analyses were undertaken over new SIMS U–Pb spot analyses reported herein. Initial $^{176}Hf/^{177}Hf$ ratios were calculated using a ^{176}Lu decay constant of $1.867 \times 10^{-11} a^{-1}$ [100] and the U–Pb concordia ages from the corresponding SIMS U–Pb spot analyses. Initial $^{176}Hf/^{177}Hf$ ratios are expressed as $\varepsilon Hf_{(t)}$ values using the following values for the present-day chondritic uniform reservoir (CHUR): $^{176}Hf/^{177}Hf_{CHUR} = 0.282785$ and $^{176}Lu/^{177}Hf_{CHUR} = 0.0336$ [101]. Hf analyses with imprecise or discordant corresponding U–Pb ages, as defined in Section 3.2.4, are not drawn in the figures or used in the interpretation. The U–Pb age data from Omma et al. [34] were subject to the same filters as the new dataset (Section 3.2.4) to ensure parity between these datasets.

4. Results

4.1. Optical Petrographic Analysis

Sixty-eight samples of sandstone to coarse siltstone grain-size were point counted, comprising 65 arenites, two wackes, and a sandy limestone (Table 1). Most samples from the lower Canyon Fiord Formation are fine to coarse-grained, poorly to moderately sorted sandstones. These show compositional variability: four are sublitharenites, one is a subarkose, two are litharenites, and one is an arkose (Figure 3, Table 1). Most of the samples from the Assistance Formation are well-sorted, fine-grained sandstones. They show less compositional variability and are more quartz-rich than those from the Canyon Fiord Formation (quartz arenites and sublitharenites; Figure 3). Samples from the Trold Fiord Formation are medium-grained, moderately sorted sublitharenites and litharenites (Figure 3). Samples from the Bjorne Formation are mostly quartz arenites or quartz-rich subarkoses and sublitharenites. Samples S_HS0254, S_HS0298 and S_HS0333 (Bjorne, Roche Point or Gore Point formations) from the Lake Hazen area are coarse-grained siltstones to medium-grained sandstones that classify as sublitharenites and subarkoses (Figure 3).

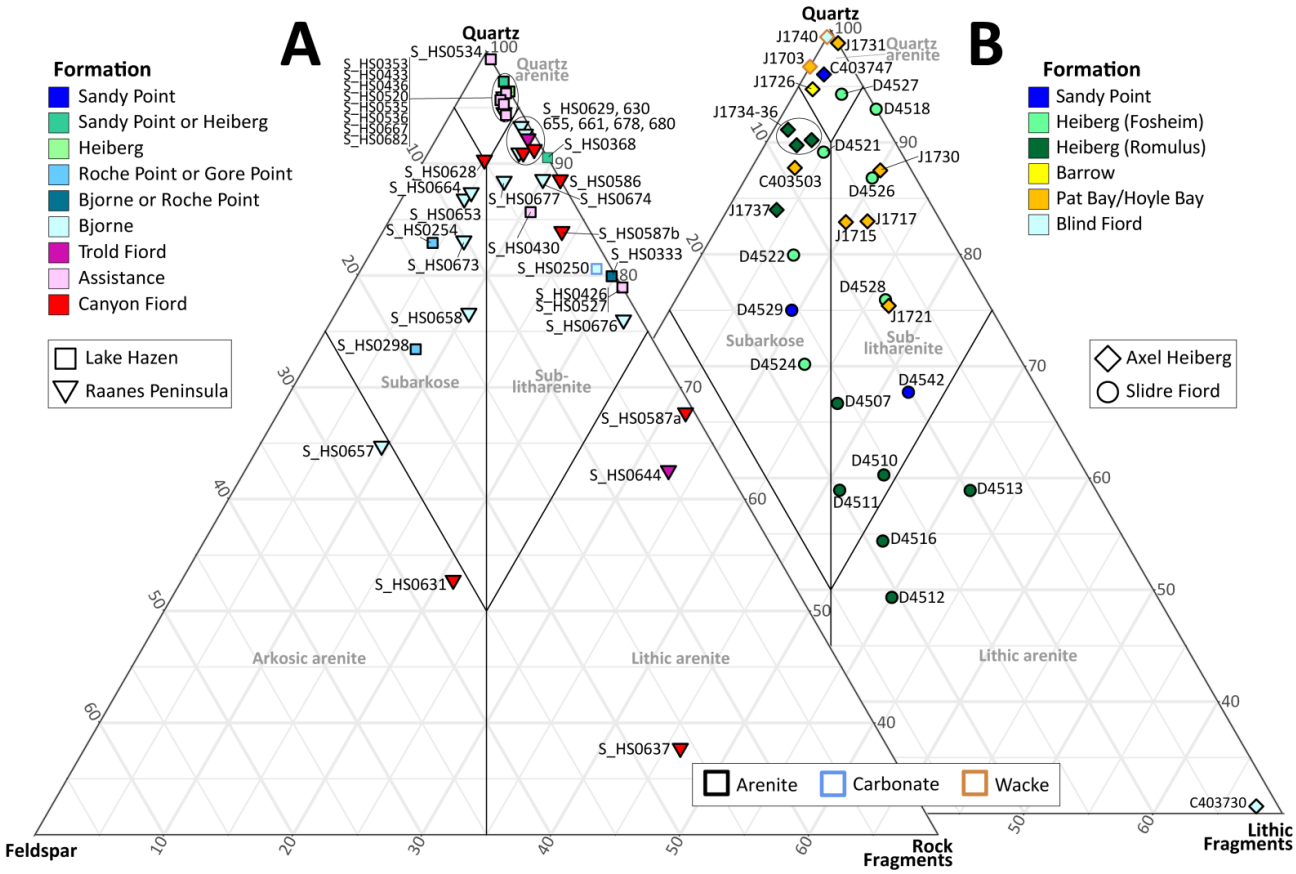

Figure 3. (**A**) Quartz–feldspar–rock fragment (QFR) ternary diagram showing point-count data collected using the traditional counting method. (**B**) Quartz–feldspar–lithic fragment (QFL) ternary diagram showing point-count data collected using the Gazzi-Dickinson method. Compositional fields are from Pettijohn et al. [89]. The figure was drawn in R using the ggtern package [102]. Note the plots are partially clipped, with the area comprising 0–30% quartz not shown.

Feldspar in all of the aforementioned samples is almost exclusively alkali feldspar (Figure 4). Rock fragments comprise mostly metamorphic types (quartz schist, quartz-mica schist, metacarbonates) and chert, with fewer carbonate and siliciclastic sedimentary rocks and vein quartz often also present.

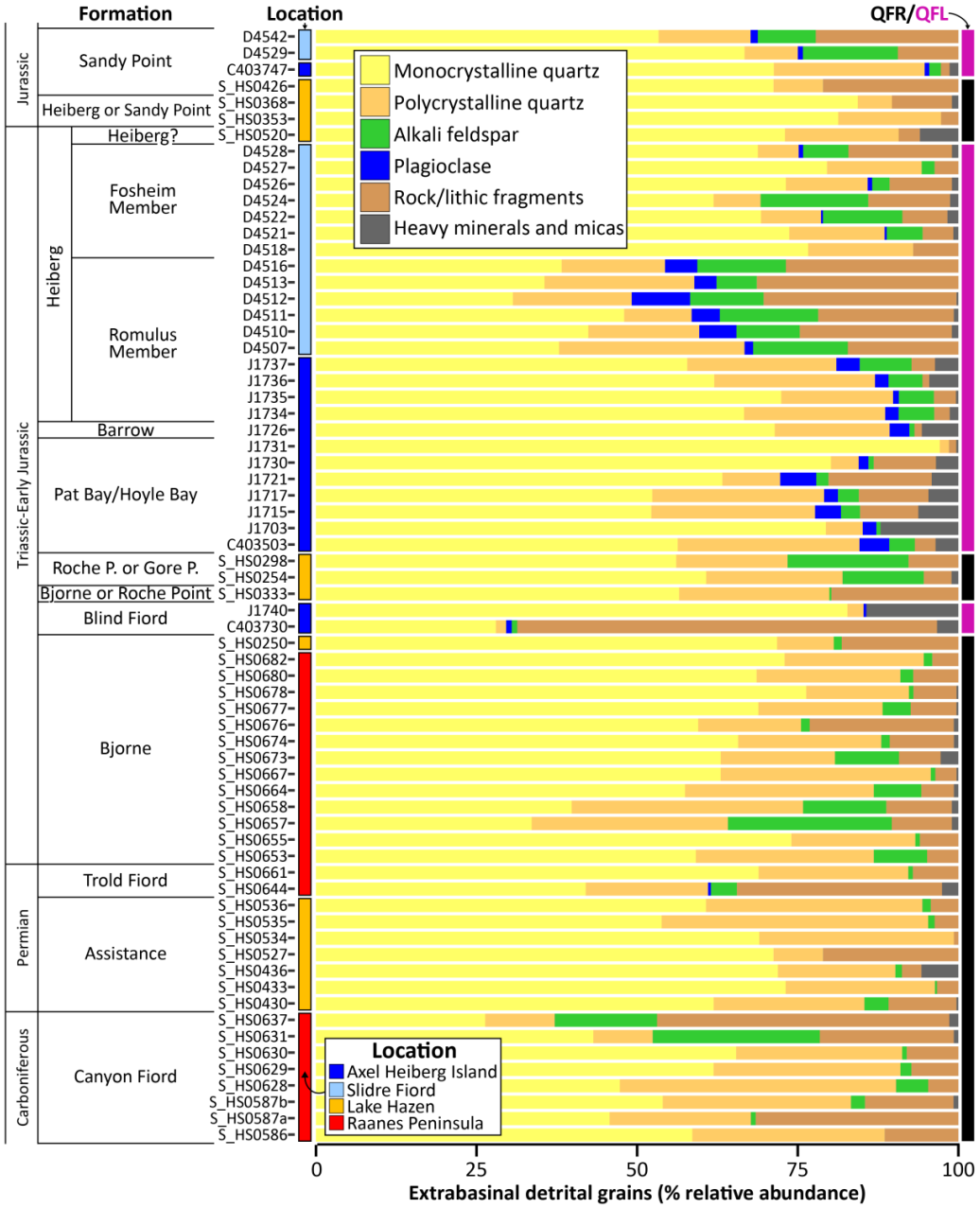

Figure 4. Summary bar charts of the petrographic point-count data. QFR = quartz, feldspar and rock fragments (traditional/Indiana method data); QFL = quartz, feldspar and lithic fragments (Gazzi-Dickinson method data).

Moderately to well sorted, siltstone to very fine sandstone samples from the Blind Fiord Formation, Hoyle Bay/Pat Bay and Barrow formations are, in contrast, marked by a generally greater abundance of plagioclase (0–5.6%, mean = 2.4%; Figure 4), which is often more abundant than alkali feldspar (0–3.9%, mean = 1.5%; Figure 4). These samples range from quartz arenites/wackes to sublitharenites and subarkoses. Lithic fragments mainly comprise mica schist and chert. Sample C403730 (Blind Fiord Formation) is a pebbly sandstone containing numerous well-rounded chert pebbles. It classifies as a litharenite (Figure 3) and contains sparse but equal amounts of plagioclase and alkali feldspar (Figure 4).

Quartz content in the Romulus Member of the Heiberg Formation varies considerably between Slidre Fiord and northern Axel Heiberg Island. Samples from northern Axel Heiberg Island are all moderately sorted, very fine to fine-grained subarkoses whereas

those from Slidre Fiord are litharenites and quartz-poor sublitharenites (Figure 3). All samples contain both plagioclase and alkali feldspar; whilst alkali feldspar is the dominant variety, plagioclase is also abundant (0.8–9.1%, mean = 3.8%; Figure 4). Lithic fragments commonly comprise schistose metamorphic types, with rare sedimentary and igneous types. Sandstone samples from the Fosheim Member at Slidre Fiord are more quartz-rich than nearby samples from the underlying Romulus Member and are more comparable to those from the Romulus Member on Axel Heiberg Island (Figure 3). These samples include subarkoses and sublitharenites, several of which are quartz rich (>85% quartz; Figures 3 and 4). Alkali feldspar (up to 16.7%) is generally much more abundant than plagioclase (<1%; Figure 4). Lithic fragments are dominated by metamorphic types, with fewer sedimentary types including chert. Three samples from the Lake Hazen area, which are probably from the Heiberg or Sandy Point formations (S_HS0520, S_HS0353 and S_HS0363) are quartz arenites or quartz-rich sublitharenites that lack feldspar and contain sparse metamorphic, siliciclastic sedimentary and chert rock fragments (Figures 3 and 4). Sample S_HS0353 also contains rare igneous rock fragments.

Sample S_HS0426 from the Sandy Point Formation in the Lake Hazen area is a very poorly sorted, coarse-grained sublitharenite that lacks feldspar. Samples from the same formation on northern Axel Heiberg Island and at Slidre Fiord are moderately sorted to well sorted, very fine to fine-grained quartz arenites and sublitharenites that contain a mixture of alkali feldspar and plagioclase, with the former being more abundant (C403747, D4529 and D4542; Figure 4). Samples D4529 and D4542 are glauconitic. Lithic/rock fragments in all samples comprise mostly metamorphic and sedimentary types including chert. Sample D4542 also contains rare igneous lithic fragments.

4.2. Conventional Heavy Mineral Analyses

The transparent heavy mineral assemblages from 70 samples were counted (Table 1). Samples from the Canyon Fiord, Assistance, Trold Fiord and Bjorne Formations, as well as two samples from the Bjorne, Roche Point or Gore Point formations near Lake Hazen (S_HS0254 and S_HS0333), generally have assemblages dominated by zircon, tourmaline and rutile (65–99.5%, mean = 88.7%) and are characterised by low ATi (mostly <20), GZi (mostly <3) and CZi (<2) values (Figure 5). Apatite (0–32.5%), garnet (0–11.2%) and staurolite (0–12%) are present in a number of samples, particularly those from the Canyon Fiord and Bjorne formations. These compositional variations are also manifest as modest increases in the ATi (up to 55) and GZi (up to 25.4) values (Figure 5). RuZi values from these samples, and the dataset as a whole, largely range from 7 to 28 and show no obvious stratigraphic or geographic variation (Figure 5). As such, RuZi values are not discussed in detail.

Sample S_HS0298 (Roche Point or Gore Point formations) is apatite rich (51%), as are samples from the Pat Bay/Hoyle Bay and Barrow formations, and from the Romulus Member of the Heiberg Formation (18–93%, mean = 51.7%). Several of these samples also contain chrome spinel (0–7.4%) and chloritoid (0–15.9%). Unsurprisingly, these samples are characterised by very high ATi (>52.5) and variable CZi (0–16.3, mean = 6.2) values (Figure 5). Sample S_HS0113 additionally contains a sizeable proportion of clinopyroxene (14.5%).

Samples of the Fosheim Member of the Heiberg Formation from Slidre Fiord have ultrastable heavy mineral assemblages dominated by zircon, tourmaline, rutile grains (>94.8%; Figure 5). Undifferentiated Heiberg Formation samples have similarly ultrastable assemblages (96–97% ZTR; Figure 5). Apart from S_PH0292, undifferentiated Heiberg Formation samples from Sawtooth Range additionally contain a small amount of garnet (9–17%), which is often accompanied by trace to small amounts of staurolite (0–6.5%), and trace amounts of monazite (0–1.5%; Figure 5). This is reflected in the GZi (10.7–37) and MZi (0–2.9) values from these samples (Figure 5). Three samples from the Heiberg or Sandy Point formations collected near Lake Hazen (S_HS0520, S_HS0353 and S_HS0368) have ultrastable assemblages dominated by zircon, tourmaline and rutile ($\geq$97%; Figure 5).

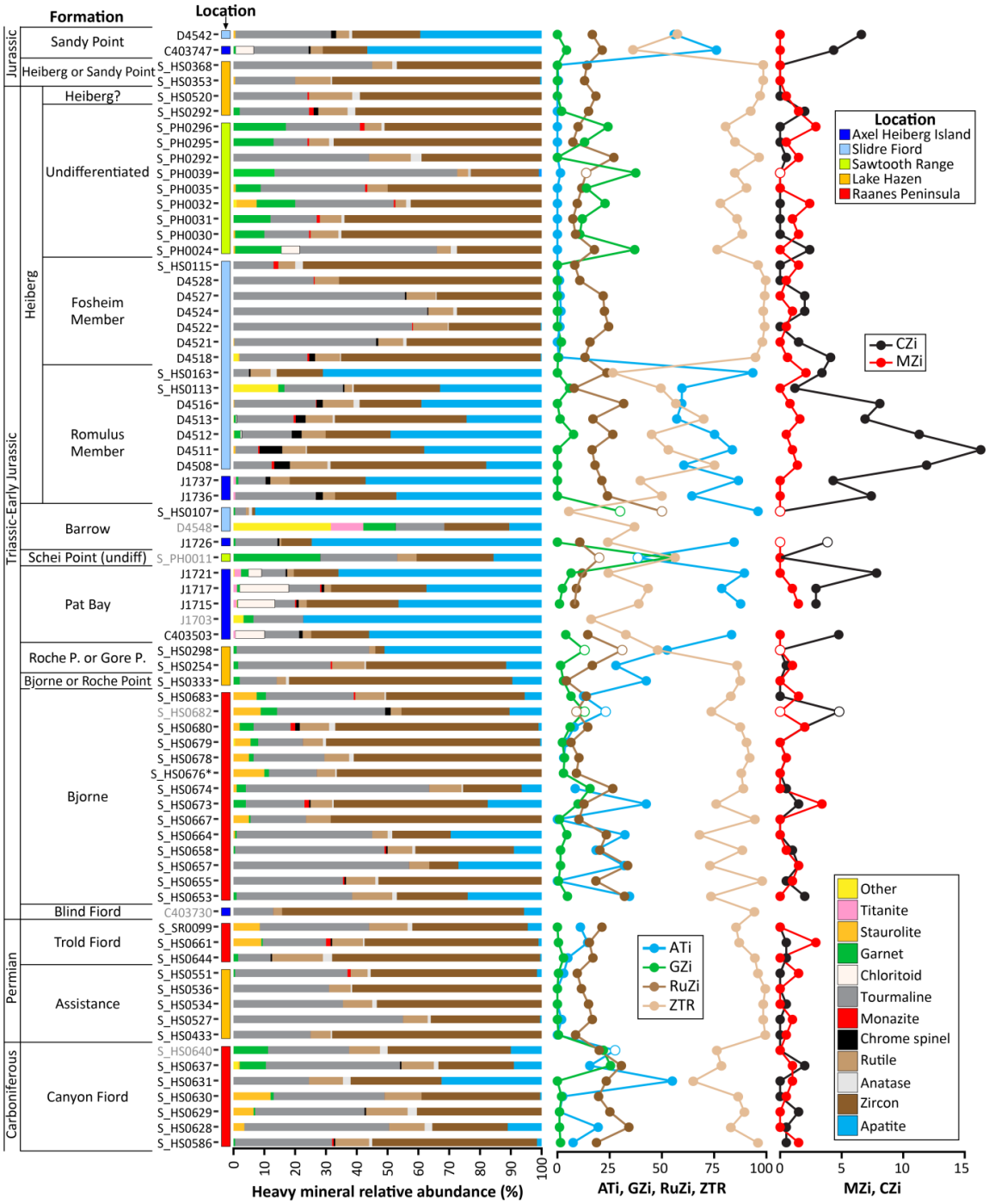

Figure 5. Conventional heavy mineral data. The relative abundances of the transparent heavy minerals are illustrated as bar charts. Sample numbers in grey indicate assemblages based on <100 counts. *Sample S_HS0676 was treated with hydrochloric acid prior to counting because of overwhelming amounts of carbonate minerals; unfortunately, this treatment also removed phosphate minerals including apatite. Minerals plotted as "other" comprise calcic amphibole, clinopyroxene, epidote, gahnite, kyanite and orthopyroxene. Provenance sensitive indices are illustrated as line graphs. ATi = apatite:tourmaline index, GZi = garnet:zircon index, RuZi = rutile:zircon index, MZi = monazite:zircon index and CZi = chrome spinel:zircon index (after [91]). ZTR index = sum of zircon, tourmaline and rutile as a percentage of total transparent heavy minerals. Open circles denote provenance sensitive index values based on fewer than 30 counts. Data from samples C403730, C403503 and C403747 are redrawn from Omma et al. [34].

Samples from the Sandy Point Formation from northern Axel Heiberg Island (C403747; [34]) and Slidre Fiord (D4542) contain a high proportion of apatite (39.4–56.6%) and small amounts of chrome spinel (<2%; Figure 5). These have high ATi (56–76.1) and CZi (4.3–6.6) values (Figure 5).

4.3. Apatite Chemistry

The trace element chemistry of apatite grains from fourteen samples was determined (Table 1), with between 49 and 62 grains analysed per sample. Samples from the Canyon Fiord through to the Roche Point or Gore Point formations, apart from sample S_HS0333, contain similar proportions of apatite grains potentially derived from high-grade metamorphic, leucosome and anatectic rocks (HM; 25–38%; Figure 6). They, however, show variations in the amount of grains potentially derived from low- and medium-grade metamorphic and metasomatised rocks (LM), grains potentially derived from felsic granitoids (S), and grains potentially derived from ultramafic igneous rocks (UM; Figure 6).

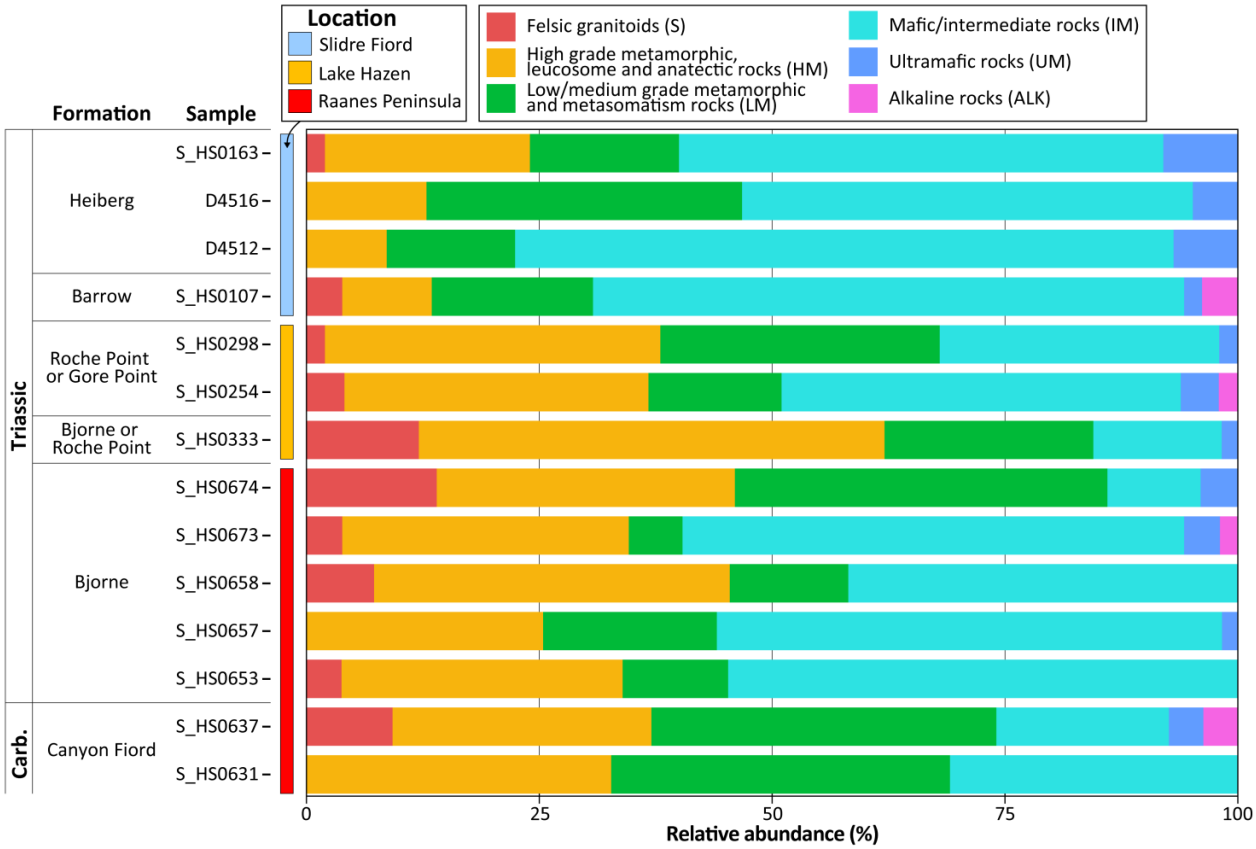

Figure 6. Bar chart summarising the likely source rocks from which the apatite grains were derived. Grains were classified based on their trace element chemistry following O'Sullivan et al. [92].

Two samples from the Canyon Fiord Formation (S_HS0631 and 0637) are characterised by a high proportion of LM-type grains (36–37%); sample S_HS0637 additionally contains a notable amount of S-type grains (9%; Figure 6). Four out of five samples from the Bjorne Formation yielded similar apatite assemblages (S_HS0653, 657, 658 and 673) characterised by a large proportion of IM-type grains (41–55%), together with fewer LM-type (6–19%) and S-type grains (0–7%). The fifth sample from the Bjorne Formation (S_HS0674), in contrast, contains very few IM-type apatite grains (10%) and larger proportions of LM-type (40%) and S-type grains (14%; Figure 6). Sample S_HS0333 from the Bjorne or Roche Point formations is also characterised by few IM grains (13.8%) and instead contains the largest proportion of HM-type grains of all the samples analysed (50%; Figure 6). Two samples from the Roche Point or Gore Point formations contain intermediate amounts

of LM- (14–30%) and IM-type (30–43%) grains compared to the older samples analysed. Samples from the Barrow Formation and the Romulus Member of the Heiberg Formation are characterised by a very large proportion of IM-type grains (48–71%) and much smaller proportions of HM-type grains compared to the older samples analysed (<22%; Figure 6).

4.4. Garnet Chemistry

The major element chemistry of garnet grains from four samples was determined (Table 1), with fifty grains analysed from each sample. The vast majority of garnet grains classify as being of metamorphic origin (74–96%; Figure 7). Most of these are inferred as being derived from intermediate/felsic metaigneous rocks or metasedimentary rocks, although grains from metamafic rocks are present in small amounts in all four samples (Figure 7). The latter classify predominantly as eclogite/ultra-high pressure (UHP) facies. Samples S_HS0637 and S_HS0673 contain larger proportions of igneous grains than the other two samples. All of the igneous grains recorded are inferred to originate from intermediate to felsic rocks.

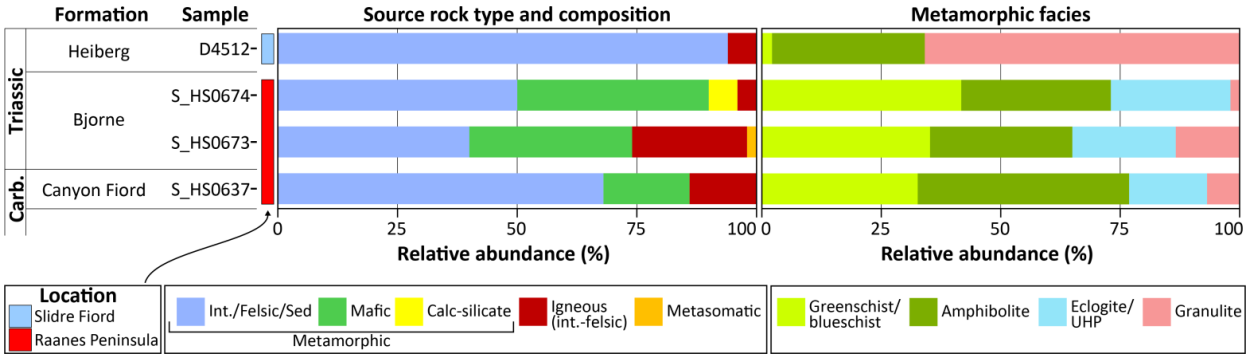

Figure 7. Bar chart summarising the likely source rocks from which the garnet grains were derived. Grains were classified based on their major element chemistry following Schönig et al. [95]. Fifty grains were analysed from each sample. Int = intermediate; Sed = sedimentary; UHP = ultra-high pressure.

Metamorphic grains in samples S_HS0637, 673 and 674 (Canyon Fiord and Bjorne formations) show a much greater range of facies and composition compared to sample D4512 from the Romulus Member (Figure 7). These three samples are characterised by broadly equal amounts of greenschist/blueschist and amphibolite-facies grains, fewer eclogite/UHP grains, and sparse granulite grains. They are also characterised by a higher proportion of mafic metamorphic grains than sample D4512. Sample D4512 is, in contrast, characterised by a much greater proportion of granulite-facies grains (Figure 7).

4.5. Rutile Chemistry

Rutile grains from 27 samples were analysed for their trace element chemistry (Table 1), with between 46 and 60 grains analysed per sample. Metapelitic grains are more abundant than metamafic grains in all of the samples analysed (60–89% of grains; Figure 8). In detail, Carboniferous to Early Jurassic samples from the Canyon Fiord to Heiberg formations are dominated by amphibolite-facies grains (59–96% of grains, mean = 82.5%; Figure 8). Lower amphibolite-facies metapelitic grains are particularly well represented (22–52% of grains, mean = 37.6%; Figure 8). In contrast, sample S_HS0353 from the Heiberg or Sandy Point formations is characterised by a much larger proportion of granulite-facies grains (60%), together with fewer amphibolite-facies grains (37.5%; Figure 8).

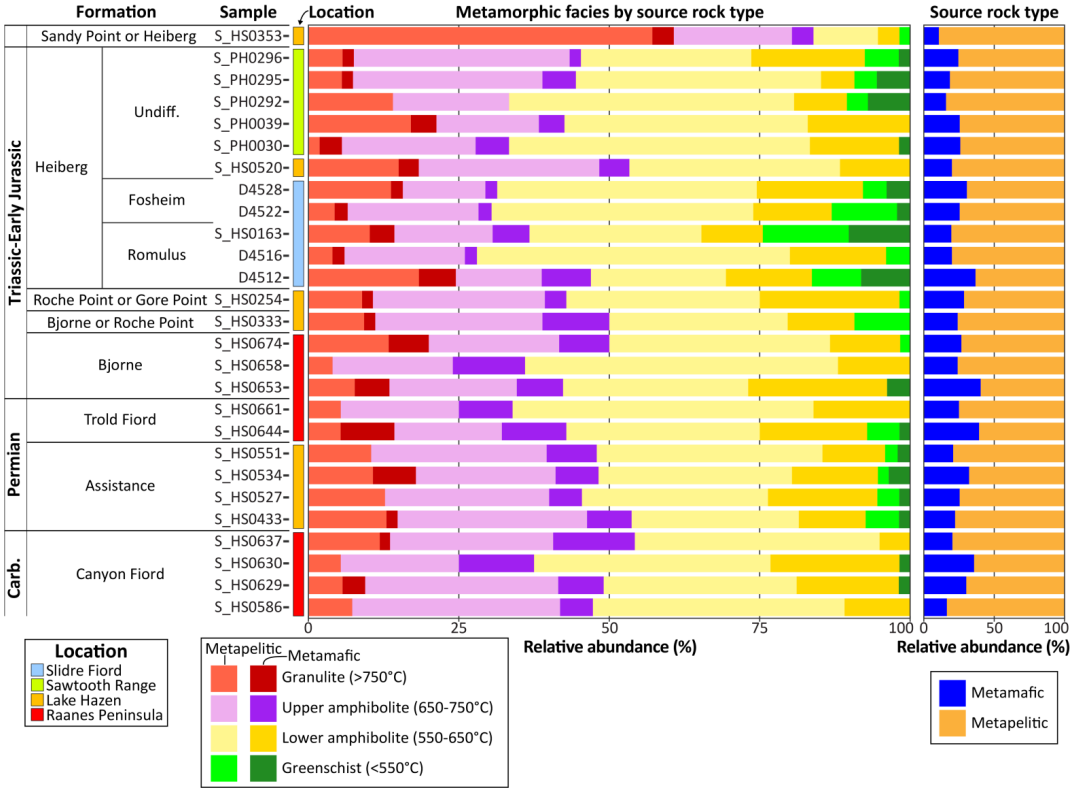

Figure 8. Bar chart summarising the likely source rocks and metamorphic grade from which the rutile grains were derived. Grains were classified into metapelite and metamafic types based on Cr and Nb concentrations following Meinhold et al. [93]. Temperatures were estimated using the Zr-in-rutile thermometer [94] and grouped into metamorphic facies. Undiff. = undifferentiated.

4.6. Detrital Zircon U–Pb Geochronology

New U–Pb detrital zircon age data have been obtained from 19 samples (Table 1). Additional SIMS analyses were also undertaken on sample C403730 (Blind Fiord Formation), supplementing the dataset of Omma et al. [34]. Carboniferous to Early Triassic samples from the Canyon Fiord, Assistance, Trold Fiord and Bjorne formations are dominated by *c*. 950–2100 Ma grains, together with sparse *c*. 2500–2800 Ma grains (Figure 9). Most of these samples also contain sparse *c*. 390–470 Ma grains. Omma et al. [34] reported an age spectrum from sample C403730 (Blind Fiord Formation) comprising a narrow *c*. 265–290 Ma age population, together with sparse, scattered *c*. 950–1641 Ma grains and a single Archean (3108 Ma) grain. Additional SIMS analyses were undertaken on grains picked from the same heavy mineral separate as used by Omma et al. [34] and yielded similar ages. The two datasets are combined in Figure 10. Sample S_HS0254 from the Roche Point or Gore Point formations has a similar detrital zircon spectrum to the samples from the Canyon Fiord to Bjorne formations (Figure 9). In contrast, samples from the Pat Bay/Hoyle Bay formations (J1717) and Romulus Member of the Heiberg Formation (J1737) on northern Axel Heiberg Island have age spectra characterised by *c*. 215–470 Ma ages with very few older grains (Figure 10). Several grains in these samples overlap within uncertainty with the depositional age ranges of the respective lithostratigraphic units (Figure 10). Samples from the Romulus Member near Slidre Fiord (D4508 and D4512) also contain large proportions of young (*c*. 224–480 Ma) grains. These are, however, accompanied by larger proportions of older (*c*. 680–2891 Ma) grains compared to sample J1737 (Figure 10). The older grains occur scattered across a wide range of ages, with no clear age populations. Samples from the Fosheim Member (D4521 and D4528) and undifferentiated Heiberg Formation samples from the Sawtooth Range (S_PH0030, S_PH0292) are dominated by *c*. 950–2100 Ma grains, together with sparse *c*. 395–470 Ma and scattered Archean (*c*. 2518–3223 Ma) grains

(Figures 9 and 10). Sample S_HS0353 from the Heiberg or Sandy Point formations in the Lake Hazen area yielded a similar age spectrum (Figure 9). Sample D4542 from the Sandy Point Formation near Slidre Fiord is characterised by sizeable *c*. 207–480, 545–600 and 640–690 Ma age groups, together with sparse scattered *c*. 700–1960 and 2300–2600 Ma grains (Figure 10). The sample was initially analysed using LA-ICPMS, which yielded one grain close to the late Toarcian to Aalenian depositional age of the Sandy Point Formation (180.1 ± 3.5 Ma, 2s, Toarcian). Subsequent SIMS analysis on grains taken from the same heavy mineral separate, however, failed to identify more Early Jurassic grains. The youngest reliable grains in this sample are early Rhaetian and older (>207.3 Ma).

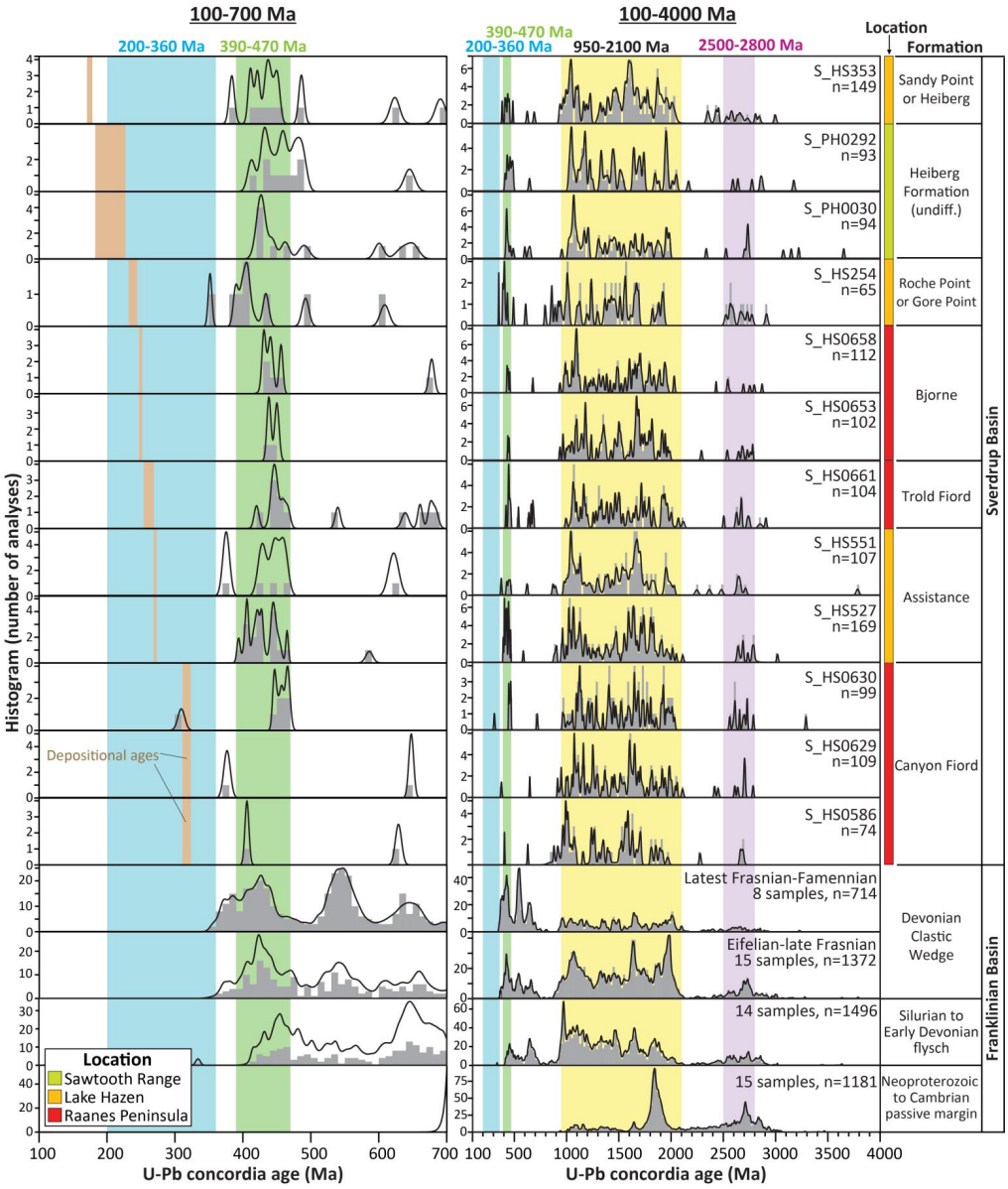

Figure 9. Combined probability density plots and histograms showing the detrital zircon U–Pb age data obtained from Late Carboniferous to Jurassic samples analysed from the southern margin of the Sverdrup Basin. Only data that are <10% discordant are shown. Approximate depositional ages shown in the left-hand panel (brown bars) are from Figure 2 with stratigraphic ranges referenced to Cohen et al. [70]. The histogram bin width is 10 and 20 Ma in the left- and right-hand columns, respectively. Published data from the Franklinian Basin succession are from Anfinson et al. [42,43], Beranek et al. [47,58], Hadlari et al. [57], and Malone et al. [50].

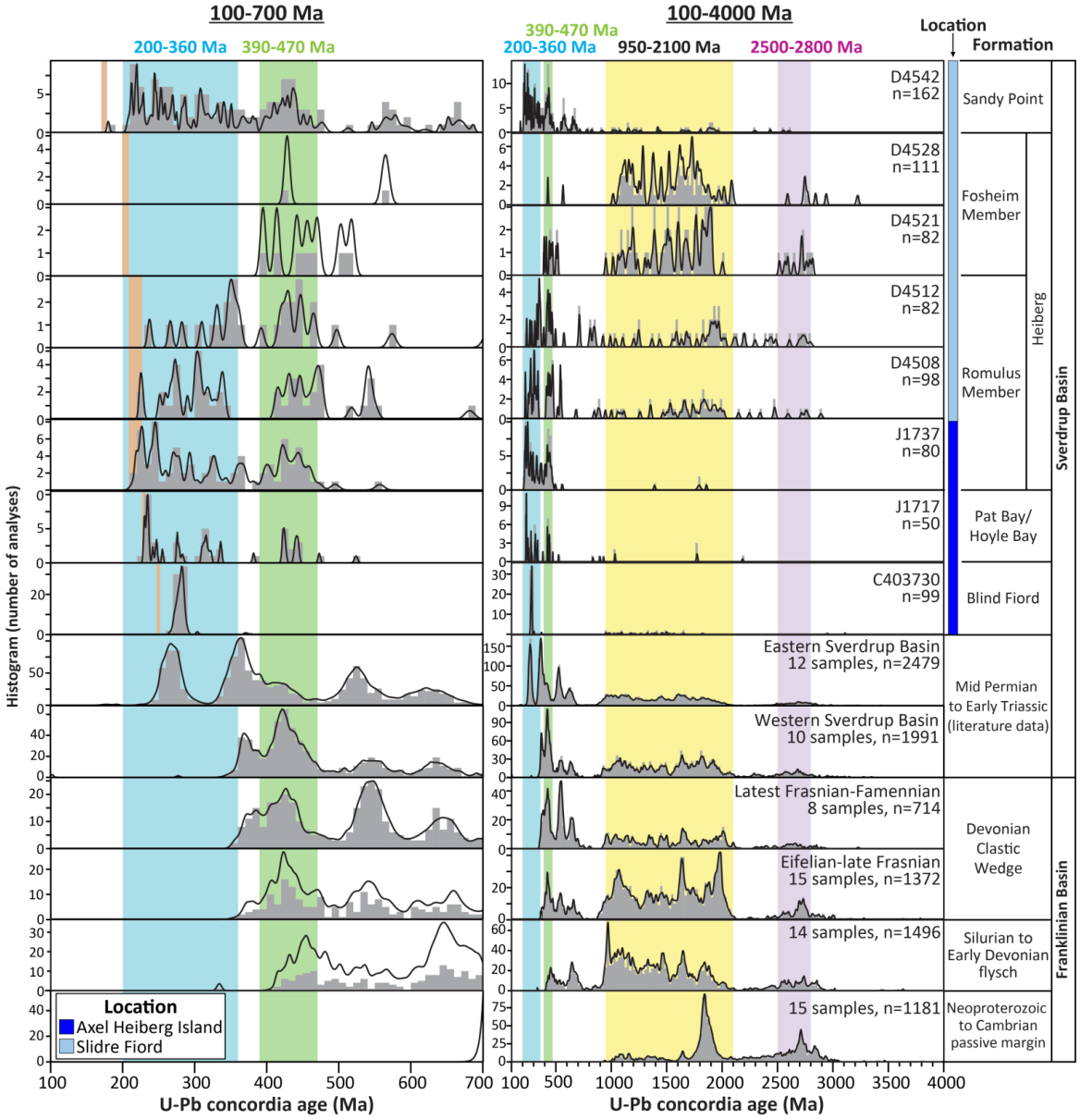

Figure 10. Combined probability density plots and histograms showing the detrital zircon U–Pb age data obtained from Triassic to Middle Jurassic samples analysed from the northern margin and axial areas of the Sverdrup Basin. Approximate depositional ages shown in the left-hand panel (brown bars) are from Figure 2 with stratigraphic ranges referenced to Cohen et al. [70]. The histogram bin width is 10 and 20 Ma in the left- and right-hand columns, respectively. The spectrum from sample C403730 includes reprocessed data from Omma et al. [34]. Published data from Middle Permian to Early Triassic strata are from Alonso-Torres et al. [15], Anfinson et al. [32], Galloway et al. [31] and Hadlari et al. [30]. Data from the Franklinian Basin succession are the same as those drawn in Figure 9.

4.7. Detrital Zircon Hafnium Isotopes

Zircon grains from sample C403730 (Blind Fiord Formation), as well as samples from the Pat Bay/Hoyle Bay (C403503, J1717), Heiberg (Romulus Member; J1737), and Sandy Point formations (D4542, C403747) were analysed for Lu–Hf isotopes (Table 1; Figures 11 and 12). Most of the grains analysed are <500 Ma. Older grains in these samples yielded scattered ages and $\varepsilon Hf_{(t)}$ values that are, for the most part, not discussed in detail.

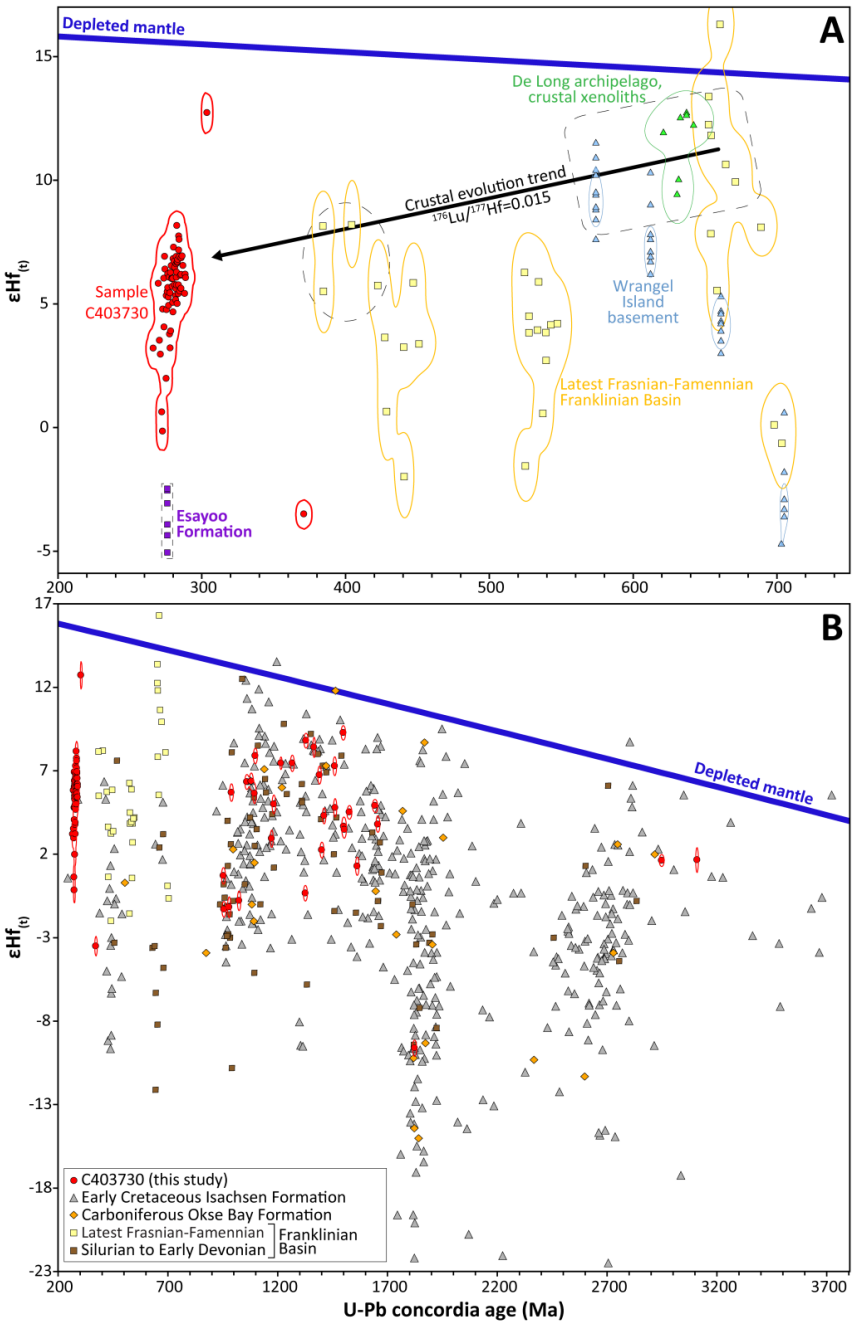

Figure 11. U–Pb age versus $\varepsilon Hf_{(t)}$ scatter plots showing data from sample C403730. (**A**) plot focusing on the dominant Permian age population in this sample; (**B**) plot showing the less abundant older grains. Data from the Esayoo Formation are whole-rock $\varepsilon Nd_{(t)}$ data from Morris [67] that are converted to approximate $\varepsilon Hf_{(t)}$ values using the εNd–εHf terrestrial array relationship of Vervoort et al. [103]. Detrital zircon U–Pb age and Lu–Hf isotope data from the Franklinian Basin [43,50], Okse Bay Formation [50] and Isachsen Formation [104] were reprocessed using U–Pb concordia ages. Analyses with U–Pb ages >10% discordant are not shown. Detrital zircon U–Pb age and Lu–Hf isotope data from basement rocks on Wrangel Island are from Gottlieb et al. [105]. Detrital zircon U–Pb age and Lu–Hf isotope data from crustal xenoliths from basalts on the De Long Islands are from Akinin et al. [106]. The thin bands surrounding data points are two-dimensional probability distributions drawn from the data and their respective analytical uncertainties in R using code modified from Sircombe [107]; they are drawn at the 2s confidence level. The depleted mantle trend is drawn assuming a present-day composition of $^{176}Lu/^{177}Hf$ = 0.0384 and $^{176}Hf/^{177}Hf$ = 0.28325 [108].

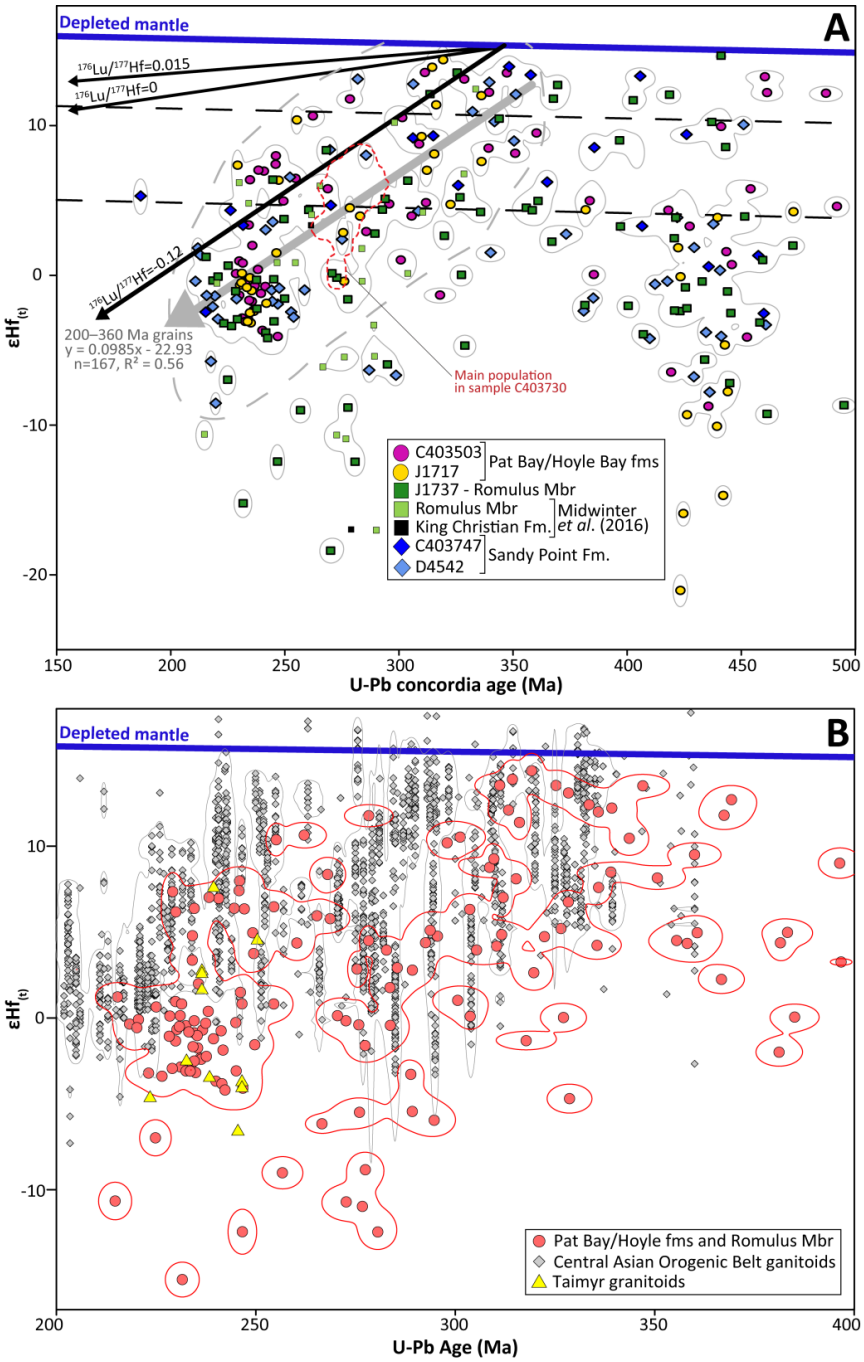

Figure 12. (**A**) U–Pb age versus $\varepsilon Hf_{(t)}$ scatter plot showing data from the Pat Bay, Hoyle Bay, Heiberg, King Christian and Sandy point formations. Detrital zircon Hf isotope data from Midwinter et al. [33] were reprocessed using U–Pb concordia ages. Analyses with U–Pb ages >10% discordant are not shown. (**B**) U–Pb age versus $\varepsilon Hf_{(t)}$ scatter plot showing data from Late Triassic strata of the Sverdrup Basin (this study and [33]), Carboniferous to Triassic granitoids of the Central Asian Orogenic Belt [109–136] and Triassic granitoids on Taimyr [137,138]. Data from the Taimyr granitoids are whole-rock $\varepsilon Nd_{(t)}$ data are converted to approximate $\varepsilon Hf_{(t)}$ values using the εNd–εHf terrestrial array relationship of Vervoort et al. [103]. In both plots, the thin bands surrounding data points are two-dimensional probability distributions drawn from the data and their respective analytical uncertainties in R using code modified from Sircombe [107]; they are drawn at the 2s confidence level. The depleted mantle trend is drawn assuming a present-day composition of $^{176}Lu/^{177}Hf = 0.0384$ and $^{176}Hf/^{177}Hf = 0.28325$ [108]. Mbr = member; Fm/fms = Formation/formations.

One hundred and eight Lu–Hf isotope analyses were undertaken on grains from sample C403730 (Blind Fiord Formation), of which 99 analyses have robust corresponding U–Pb ages (Figure 11). 266–288 Ma zircons, which comprise the majority of the analysed grains in this sample, yield $\varepsilon Hf_{(t)}$ values of −0.2 to +8.2, although most are strongly clustered around +6 (Figure 11a). 952–1822 Ma zircons yield $\varepsilon Hf_{(t)}$ values of −1.3 to +9.3 (Figure 11b).

The majority of Carboniferous to Triassic zircons in samples analysed from the Pat Bay, Hoyle Bay, Heiberg and Sandy Point formations show a positive trend between U–Pb age and $\varepsilon Hf_{(t)}$ values, with juvenile values (up to +14.4) in the *c.* 330–360 Ma grains to more evolved, sub-CHUR $\varepsilon Hf_{(t)}$ values (roughly −4 to +1) in the *c.* 215–245 Ma grains (Figure 12a). Sample J1737 additionally contains several Carboniferous-Triassic grains yielding more evolved $\varepsilon Hf_{(t)}$ values that lie below the main trend (down to −18.4) and are not represented in either of the samples from the Pat Bay/Hoyle Bay formations. Sample D4542 from the Sandy Point Formation contains two *c.* 285–300 Ma grains with −6 to −7 $\varepsilon Hf_{(t)}$ values. These are similar to the more evolved grains in sample J1737.

Samples J1717 and C403503 show some similarities and differences in the $\varepsilon Hf_{(t)}$ values from their *c.* 420–500 Ma detrital zircons. Both samples contain *c.* 418–452 Ma grains with −8.7 to +4.3 $\varepsilon Hf_{(t)}$ values. Sample J1717 additionally contains a number of very evolved *c.* 426–442 Ma grains (−9 to −21), whilst sample C403503 contains a number of *c.* 454–492 Ma grains with more juvenile $\varepsilon Hf_{(t)}$ values (+4.6 to +13.2) that are poorly represented in sample C403503. 396–472 Ma zircon grains in samples J1737, C403747 and D4542 yield similar wide ranges of $\varepsilon Hf_{(t)}$ values from −9.3 to +14.7 that show no correlation with the corresponding U–Pb ages (Figure 12a).

5. Discussion

5.1. Carboniferous to Earliest Late Triassic Sediment Supply on the Southern Basin Margin

Samples from the Canyon Fiord, Assistance, Trold Fiord and Bjorne formations on the Raanes Peninsula and near Lake Hazen, as well as Early Triassic to early Carnian samples from the latter area (S_HS0250, 254, 298 and 333; Figure 2), are compositionally similar. Many of these samples are relatively compositionally mature (>80% quartz; Figure 3), contain only alkali feldspar and have rock fragment assemblages dominated by metasedimentary and sedimentary types. They also have heavy mineral assemblages largely comprising zircon, tourmaline and rutile, and have detrital zircon U–Pb spectra dominated by *c.* 950–2100 Ma ages (Figures 5 and 9). Collectively, these data suggest a predominantly recycled (sedimentary/metasedimentary) provenance. Garnet and staurolite are present in small amounts in several samples from the Canyon Fiord, Trold Fiord and Bjorne formations (Figure 5), which when combined with the chemical analysis of the garnet and rutile grains suggests that they were predominantly derived from amphibolite-facies metasedimentary rocks (Figures 7 and 8).

Strata of the lower Canyon Fiord Formation are inferred as being locally sourced from fault blocks bounding the actively rifting subbasins [63,71,79]. This is consistent with the coarse grain size and textural immaturity of the analysed samples. Strata within the Trold Fiord depression (Figure 1c) have yielded west- and northwest-directed palaeocurrent indicators, which are interpreted to indicate flow from the graben flank towards the main axial drainage network. Thorsteinsson [71] observed that the clast composition of conglomeratic units within the formation reflects spatial compositional variations in the local Franklinian basement. The three samples analysed for detrital zircon U–Pb geochronology have age spectra that are very similar to spectra from Silurian and younger strata within the Franklinian Basin succession (Figures 9 and 13). These sediments are interpreted as being derived predominantly from the Greenland and Svalbard Caledonides, and Pearya [42,43]. 500–700 Ma grains dominate several samples analysed from latest Frasnian to Famennian strata of the Devonian clastic wedge (Figures 9 and 13) but occur more sporadically in the underlying Silurian to late Frasnian parts of the Franklinian Basin succession [42,43,58]. Such Neoproterozoic grains are poorly represented in the lower

Canyon Fiord Formation samples and so these samples were more likely derived from the Silurian to late Frasnian part of the Franklinian Basin succession.

The close similarity in composition of samples from the Assistance, Trold Fiord, Bjorne, Roche Point and Gore Point formations compared to those from the lower Canyon Fiord Formation supports a shared provenance. This is chiefly from the Silurian to late Frasnian parts of the Franklinian Basin succession. Published thickness and facies trends, and palaeocurrent measurements from the main part of the basin (i.e., southeast of the Tanquary High; Figure 1c) support that sediment was supplied from the south and/or east [16,18–20,80,139]. In the Lake Hazen area, palaeocurrent vectors measured from fluvial/floodplain to proximal shelf facies of the Assistance Formation indicate flow towards the east and northeast. This is consistent with sediment input from the Tanquary High [140,141].

Several samples from the Canyon Fiord and Bjorne formations, as well as samples S_HS0254 and S_HS0333 from the Lake Hazen area, contain sizeable amounts of apatite in their heavy mineral assemblages (up to 32.5%; Figure 5). Sample S_HS0298 (Roche Point or Gore Point formations) is an extreme case (51% apatite; Figure 5). The relative abundance of apatite in the heavy mineral assemblages is positively correlated with the abundance of alkali feldspar in the petrographic point-count dataset. The available apatite chemistry data from these samples suggest that these detrital grains were largely derived from metamorphic and mafic to intermediate igneous rocks (Figure 6). The prevalence of apatite and alkali feldspar correlates well with more arid climatic intervals. Semi-arid to arid conditions have been inferred for Late Carboniferous times as indicated, for example, by red beds and caliches in the lower Canyon Fiord Formation and the coeval deposition of evaporites in the basin centre (Otto Fiord Formation; Figure 2; [19,79,142]). The local Middle Permian climate is thought to have been more humid [142,143] and correlates with the apatite- and alkali feldspar-poor Assistance Formation (Figures 3–5). A return to more arid conditions is inferred for Early Triassic times [19,142,143], as indicated by red overbank shales and siltstones, and poorly developed caliches and paleosols within the Bjorne Formation [80]. Limited water availability during the drier intervals may have restricted the intensity of chemical weathering and permitted the recycling of less robust minerals (including apatite) from the Franklinian Basin succession.

5.2. Middle Permian to Early Triassic Sediment Supply on the Northern Basin Margin

From Middle Permian until Early Triassic times there is compelling evidence that substantial amounts of sand entered the basin from the north [15,17,23,30]. Strata on northern Axel Heiberg Island are characterised by an abundance of Permian detrital zircons [15,30,34]. This includes sample C403730 (Figure 10). The heavy mineral assemblage from this sample is dominated by zircon and apatite (Figure 5). The majority of zircon grains in this sample comprise a unimodal *c*. 265–290 Ma age population and define a restricted range of $\varepsilon Hf_{(t)}$ values (Figures 10 and 11). Collectively, the conventional heavy mineral data and the tight, unimodal clustering of the combined U–Pb and Hf isotope data suggests derivation from an area comprising Early to Middle Permian igneous rocks. The occurrence of plagioclase in samples C403730 and J1740 further supports a primary (igneous) detrital input into the Blind Fiord Formation (Figure 4). Sample C403730 also contains some *c*. 950–1641 Ma detrital zircons that overlap with the dominant age populations in Late Carboniferous to Middle Triassic samples from the southern basin margin (Figures 9 and 13). These grains yield similar $\varepsilon Hf_{(t)}$ values to coeval grains in Silurian strata of the Franklinian Basin (Figure 11b; [50]), as well as strata of the Sverdrup Basin (Okse Bay and Isachsen formations; Figure 11b) that are inferred as being sourced from the Franklinian Basin succession and/or the Canadian-Greenland Shield to the south [104,144]. Middle Permian to Early Triassic samples along the northern basin margin, in both the eastern and western parts of the basin, contain sizeable *c*. 950–2100, 500–700 and 390–450 Ma age groups (Figures 10 and 13; [15,30–32]). These age groups are compatible with the reworking Silurian to late Frasnian and latest Frasnian to Famennian units within the Franklinian Basin succession (Figure 13). Collectively, the available data suggest that the northern source area

comprised Permian igneous rocks as well as Franklinian Basin strata, as suggested by other workers [31,32,42,43].

The identity of the northern source area is poorly constrained due to the subsequent opening of the Amerasia Basin. The recognition of abundant Permian zircons in Middle Permian to Early Triassic strata of the eastern part of the Sverdrup Basin has led to suggestions that the northern source area/Crockerland formed part of a magmatic arc [15,30]. Permian detrital zircons are, however, missing from coeval sands farther to the southwest within the basin [31,32]. This was interpreted to signify a smaller scale, more local source for the magmatism and to argue against an active continental margin setting for Crockerland during this time interval [31]. The Permian zircons may be related to the outpouring of basalts and occasional pyroclastic rocks on northern Axel Heiberg and northwest Ellesmere islands, including the Kungurian Esayoo Formation. A direct link is unlikely as the Esayoo Formation has within-plate alkaline to transitional basaltic geochemistry [66] and is thus unlikely to contain abundant zircon. The possibility that these grains were derived from plutonic bodies emplaced into Crockerland during the same magmatic episode has been suggested [31]. The Esayoo Formation rocks are inferred as being derived from an enriched asthenospheric mantle source with minimal contamination from the subcontinental lithosphere and crust [66,67]. Whole-rock Sm–Nd data from the formation have yielded values of −4.0 to −5.9 $\varepsilon Nd_{(t)}$ (Morris 2013). Converting these values to approximate $\varepsilon Hf_{(t)}$ values using the εNd–εHf terrestrial array relationship of Vervoort et al. [103] yields $\varepsilon Hf_{(t)}$ values of −2.5 to −5.1. This is substantially more evolved than the $\varepsilon Hf_{(t)}$ values of *c.* 265–290 Ma detrital zircons in sample C403730 (−0.2 to +8.2; Figure 11a). The Permian zircons in sample C403730 require a more juvenile magmatic source than that inferred for the Esayoo Formation, although this magmatic episode may have provided the heat necessary to melt a more juvenile crustal source. Whole-rock Nd data from the Franklinian Basin succession indicate a detrital input from more juvenile crust to the north of the basin during late Ordovician to Devonian times [49,53]. A small number of detrital zircon Hf isotope data from the Devonian clastic wedge reveal that *c.* 380–410 and 650–675 Ma grains yield juvenile $\varepsilon Hf_{(t)}$ values up to +16 (Figure 11a; [43]). These grains are inferred to have been derived from Ellesmerian plutons and Timanide orogen affinity crust within Crockerland, respectively [31,43]. The Arctic Alaska-Chukotka microplate (AACM) contains numerous Neoproterozoic metamorphic and plutonic rocks (*c.* 550–900 Ma; [7,145,146]), which overlap in age with, and are inferred as being related to, the Timanide orogeny [7]. Neoproterozoic basement rocks on Wrangel Island and western Chukotka have yielded $\varepsilon Hf_{(t)}$ values up to +11.5 (Figure 11a; [105]). Granitic gneiss xenoliths in late Neogene to Quaternary alkali basalts on the De Long Islands, inferred to represent the local basement, have yielded similarly juvenile $\varepsilon Hf_{(t)}$ values (up to +12.7; Figure 11a; [106]). Collectively, these data demonstrate the presence of juvenile basement within the Chukotkan part of the AACM. The remelting of such crustal rocks could potentially generate the $\varepsilon Hf_{(t)}$ values measured from the *c.* 265–290 Ma detrital zircons in sample C403730 (crustal trend in Figure 11a). This is interpreted to support a detrital input from the Chukotkan part of the AACM (Figure 14a). The difference between detrital zircon age spectra of rocks from the eastern and western Sverdrup Basin may reflect spatial differences in the underlying geology of Crockerland, i.e., the Alaskan versus Chukotkan parts of the AACM, respectively (Figure 14a). These may have been separated by a drainage divide or formed discrete islands at this time.

The $\varepsilon Hf_{(t)}$ data from Early to Middle Permian zircon grains in sample C403730 also lie on the same trend as the Late Triassic samples analysed from the Pat Bay, Hoyle Bay and Heiberg formations (Figure 12a). However, there are considerable differences between the U–Pb age spectra from Middle Permian to Early Triassic samples and those from Late Triassic ones. For example, Middle Permian to Early Triassic sediments are characterised by large *c.* 250–290 and 350–370 Ma age populations and lack sizeable *c.* 300–320 and 400–450 Ma age groups unlike the Late Triassic samples (Figure 15). These differences suggest that Middle Permian to Early Triassic sands were sourced from a different area to

Late Triassic ones. As will be discussed in the Section 5.3, there is a strong argument for Late Triassic sands bearing Carboniferous to Triassic detrital zircons having been derived from the Uralian orogenic belt and/or the Arctic Uralides. However, sediment from this source had not reached Svalbard and the northwest Barents Shelf during Early to Middle Triassic times [78,147] and thus is unlikely to have overspilled into the Sverdrup Basin. Consequently, it may be coincidental that $\varepsilon Hf_{(t)}$ data from sample C403730 overlap with the trend defined by Carboniferous to Triassic detrital zircons in the Late Triassic samples. Clearly, more hafnium isotope data are needed from these northern-derived strata to characterise better their source area.

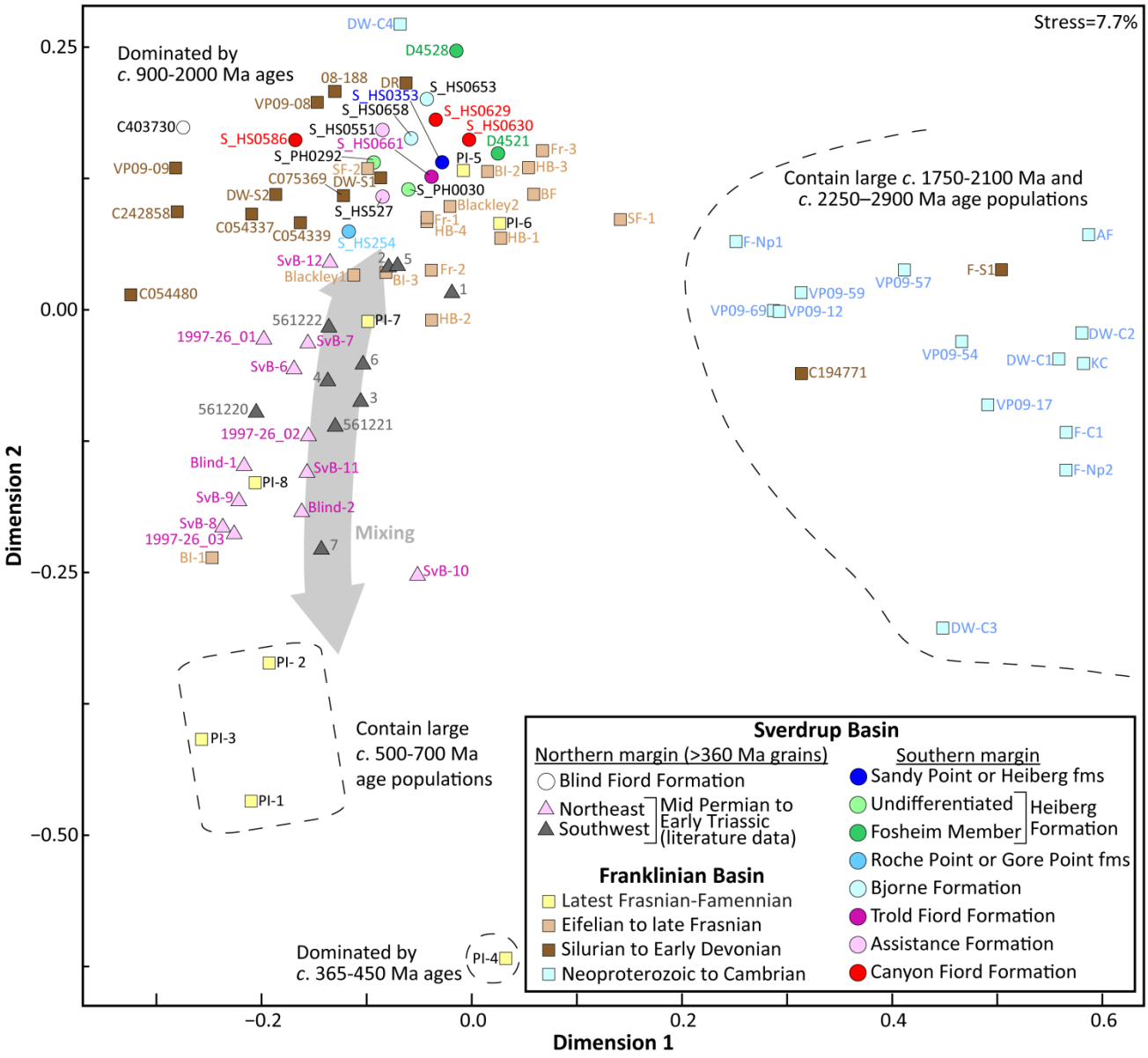

Figure 13. Multidimensional scaling plot showing the similarity/dissimilarity in detrital zircon U–Pb age spectra between Carboniferous to Middle Jurassic samples analysed from the southern margin of the Sverdrup Basin, Middle Permian to Early Triassic samples from the northern margin of the Sverdrup Basin (>360 Ma grains only), and Neoproterozoic to Devonian strata of the Franklinian Basin. Data from the Franklinian Basin succession are the same as those drawn in Figure 9. Middle Permian to Early Triassic samples from the northern margin are from Alonso-Torres et al. [15], Anfinson et al. [32], Galloway et al. [31] and Hadlari et al. [30]. The plot was drawn in R using the Provenance package [148]. Fms = formations.

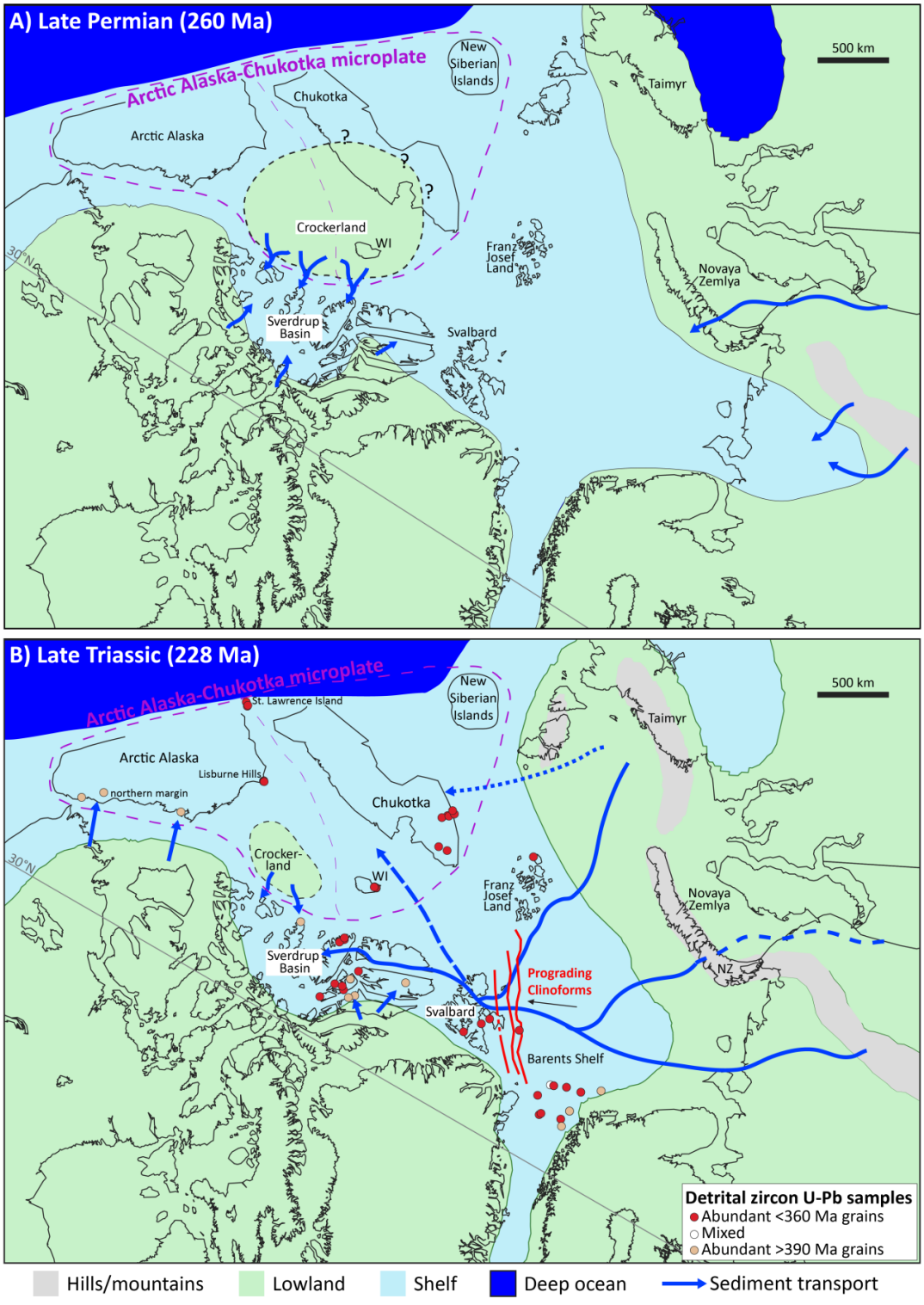

Figure 14. Simplistic regional palaeogeographic reconstructions of the Arctic region during: (**B**) Late Permian; and (**A**) Late Triassic times. The maps are modified from GPlates [149]. The palaeogeography is heavily modified from Cao et al. [150] using information in Anfinson et al. [32], Kos'ko and Korago [151], Miller et al. [7,8] and Tuchkova et al. [152]. The prograding clinoforms in (**B**) are redrawn from Gilmullina et al. [147]. Coloured circles represent new and literature samples within detrital zircon U–Pb age data. The sources of literature samples are given in Figure 15. Samples were classified into two main types (abundant <360 Ma detrital zircons and abundant >390 Ma detrital zircons) using dissimilarity analysis (Figure 16). WI = Wrangel Island.

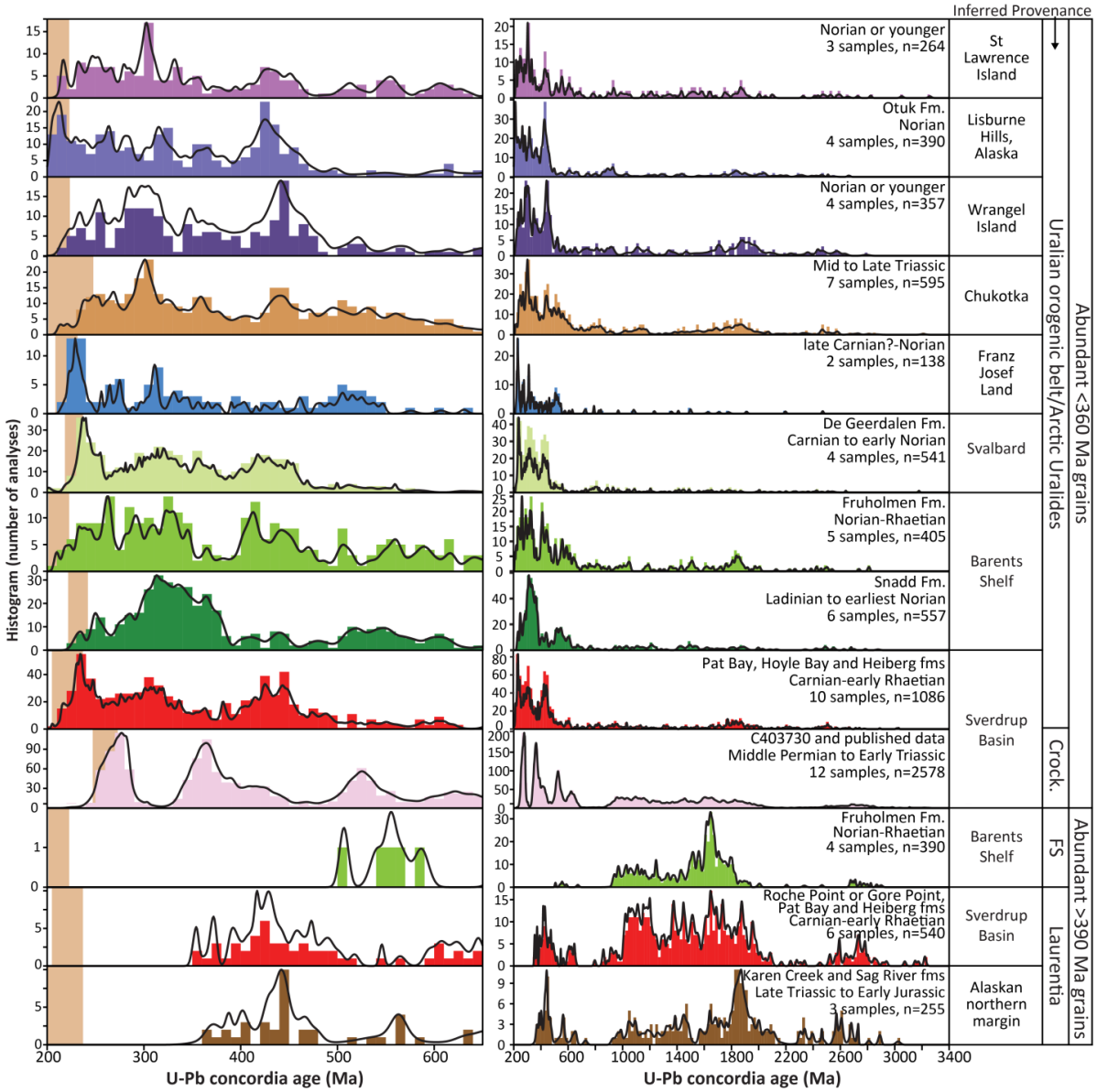

Figure 15. Combined probability density plots and histograms showing detrital zircon U–Pb age data from Middle Permian to Late Triassic strata of the Sverdrup Basin as well as Late Triassic strata from the wider Arctic region. Published data are reprocessed and drawn from the following sources: Sverdrup Basin—Alonso-Torres et al. [15], Anfinson et al. [32], Hadlari et al. [30], Midwinter et al. [33] and Omma et al. [34]; Svalbard—Pózer Bue and Andresen [153] and Klausen et al. [154]; Barents Shelf—Fleming et al. [155], Flowerdew et al. [156], Line et al. [157] and Klausen et al. [154,158]; Franz Josef Land—Soloviev et al. [159]; Chukotka—Miller et al. [10] and Amato et al. [160]; Wrangel Island—Miller et al. [8]; Lisburne Hills, Alaska—Miller et al. [10] and Dumoulin et al. [161]; St Lawrence Island—Amato et al. [162]; Alaskan northern margin—Gottlieb et al. [11]. Only data that are <10% discordant are drawn. Samples are divided into two main types based on dissimilarity analysis (abundant <360 Ma detrital zircons and abundant >390 Ma detrital zircons; Figure 16) and are then subdivided by age and region. Samples D4508, D4512, 7324/8.1_685m and 7324/9.1_711.63 have age spectra indicative of mixing between the two main types (Figure 16) and are not included in the above figure. Approximate depositional ages are shown in the left-hand panel (brown bars). Depositional ages quoted for samples from Wrangel and St Lawrence Islands are maximum values calculated from the available detrital zircon U–Pb age data using the maximum likelihood age algorithm [163]. Crock = Crockerland; FS = Fennoscandian Shield; Fm/fms = formation/formations.

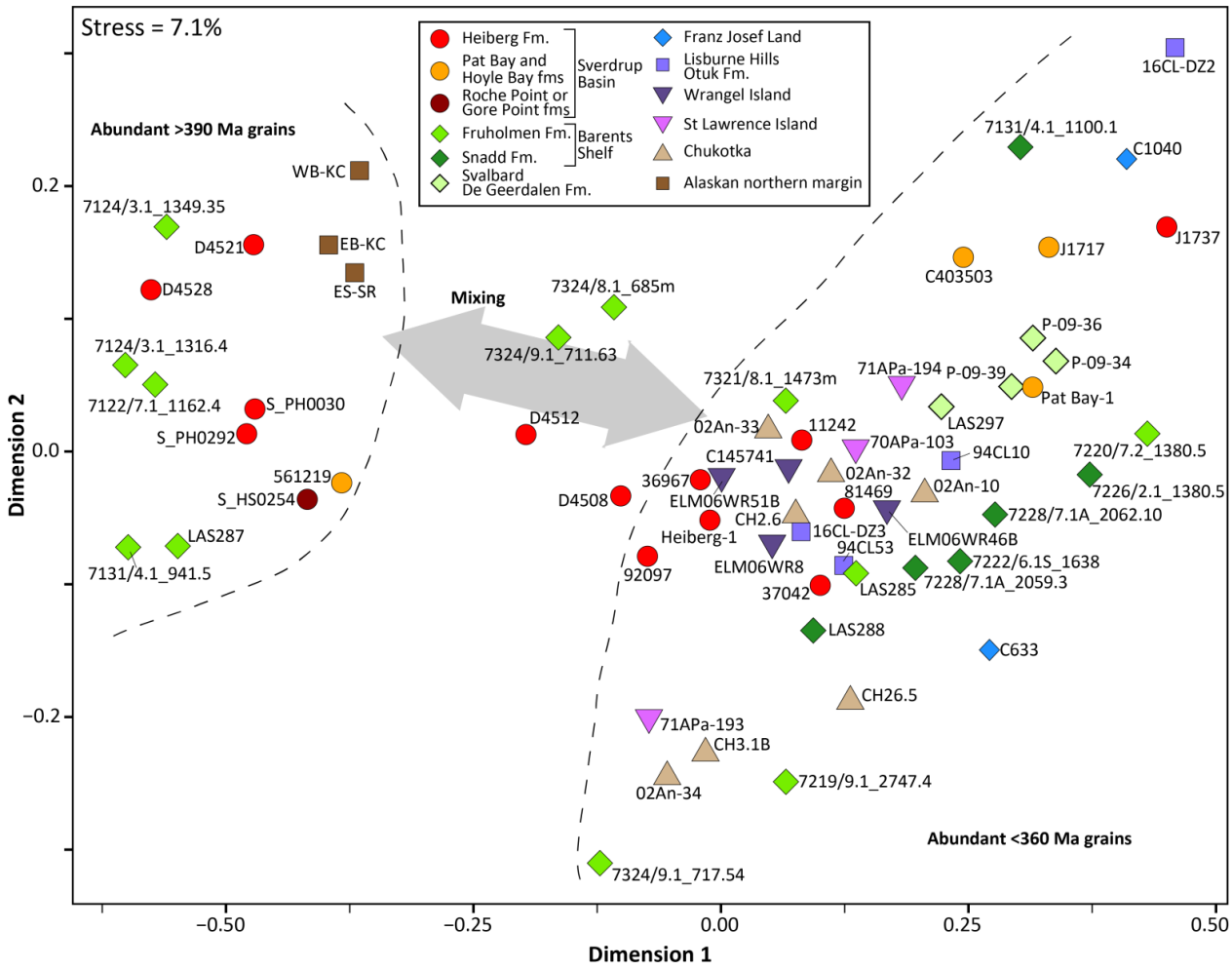

Figure 16. Multidimensional scaling plot showing the similarity/dissimilarity in detrital zircon U–Pb age spectra from Late Triassic samples of the wider Arctic region. The thick grey arrow indicates mixing between the two main sample clusters. See Figure 15 for the data sources used. The plot was drawn in R using the Provenance package [148]. Fm/fms = formation/formations.

5.3. Late Triassic Sediment Supply on the Northern Basin Margin

Sands of the Hoyle Bay and Pat Bay formations, and the Romulus Member of the Heiberg Formation mark the input of compositionally immature, apatite-rich sediment into the basin from the north (e.g., [17,23]). These samples contain plagioclase (apart from J1731) and have heavy mineral assemblages dominated by apatite, with ubiquitous small amounts of chrome spinel and chloritoid (Figure 5). Their detrital zircon age spectra are also conspicuously different to all of the older samples analysed, being characterised by a wide spectrum of Carboniferous to Ordovician (*c.* 220–485 Ma) grains, including several that are syn-depositional (Figure 10; [30,34]). Although data have been obtained from the Barrow Formation, they are few in number due to the fine grain size of the formation. However, samples S_HS0107 and J1726 are very apatite-rich and likely represent distal equivalents from the same sediment source. Samples of the Romulus Member near Slidre Fiord (D4507–D4516) are more compositionally mature than those from northern Axel Heiberg Island (J1734–1737; Figure 3). They also contain less apatite, more ultrastable minerals (zircon, tourmaline and rutile; Figure 5) and a greater proportion of >500 Ma detrital zircons (Figure 10). Apatite is, however, still comparatively abundant in these samples and chrome spinel is ubiquitous. Collectively, these data strongly suggest that in the axial areas of the basin mixing of compositionally immature northern-derived sediment and more compositionally mature southern/eastern-derived sediment occurred.

The northern-derived Sverdrup Basin samples have been inferred as being derived from Crockerland/a northern magmatic arc [17,23,30,33] or the Uralian orogenic belt/Arctic Uralides [32,34]. Late Triassic sandstone samples from the eastern Sverdrup Basin yield similar detrital zircon U–Pb age spectra to age-equivalent samples from Svalbard, the Barents Shelf, Chukotka, Wrangel Island, the Lisburne Hills of Alaska and St Lawrence Island (Figures 15 and 16). Moreover, Late Triassic sandstones deposited on the southwest Barents Shelf with a Uralian Orogen source emulate the heavy mineral assemblage recorded in the Sverdrup basin samples; i.e., one that is rich in apatite and contains chrome spinel [155]. Collectively, these data support that northern-derived Late Triassic strata in the eastern Sverdrup Basin shared a common source area with coeval strata on Svalbard, the Barents Shelf and the wider Alaska-Chukotka area.

Circa 235–250 Ma granitoids are known from Taimyr [137,138] and are a possible source for the largest U–Pb age group in these samples. Whole-rock Nd isotope data from these granitoids, when converted to approximate $\varepsilon Hf_{(t)}$ values, overlap well with the $\varepsilon Hf_{(t)}$ values of *c*. 235–250 Ma zircons in Late Triassic samples from the Sverdrup Basin (Figure 12b). The *c*. 235–250 Ma zircon population recorded from the De Geerdalen Formation [153] was also inferred by [155] to have sources within Taimyr. Alternative sources from the Central Asian Orogenic Belt have been suggested [78] and it is also possible that similarly aged units occur between Taimyr and the Polar Uralian mountains [164]. There is, however, a poor overlap in $\varepsilon Hf_{(t)}$ values between the majority of *c*. 235–250 Ma zircons in the Sverdrup Basin samples and coeval granitoids within the Central Asian orogenic belt (Figure 12b), suggesting the latter was not the source area for the former. Field studies of the De Geerdalen Formation on Svalbard have inferred that sediment was supplied from the northeast [165], east [166] and/or southeast [167]. During Triassic times, large-scale deltaic complexes prograded across the Barents Shelf from southeast towards the northwest [78,147,168–170], i.e., towards Svalbard and the Sverdrup Basin (prograding clinoforms in Figure 14b). Using a combination of seismic data and well data from the Barents Shelf, and sediment mass balance calculations, Gilmullina et al. [78] inferred that there was substantial sediment bypass/overflow from the Barents Shelf into adjacent sedimentary basins to west, northwest and north during late Carnian and Norian times. This correlates with the deposition of the Pat Bay Formation and Romulus Member in the Sverdrup Basin. Collectively, these data support that Late Triassic sandstones of the eastern Sverdrup Basin were sourced from the Uralian orogenic belt/Arctic Uralides and routed via the Barents Shelf (solid blue arrow in Figure 14b).

Based on the available detrital zircon age data, sands bearing abundant Carboniferous to Triassic detrital zircons appear earlier in the eastern Sverdrup Basin, Svalbard and Chukotka (Carnian to early Norian; Figure 15; [10,153]) than in Alaska and St Lawrence Island (Norian; [161,162]). This has been inferred to record the progradation of a sedimentary system from the northwest Barents Shelf towards Alaska (long-dashed blue arrow in Figure 14b; [171]). The available data do not preclude multiple sediment inputs, however. This may account for subtle variations within the detrital zircon U–Pb age dataset; for example, with different systems feeding Svalbard, Franz Josef Land and the Sverdrup Basin (higher abundance of Triassic grains; Figure 15; solid blue arrow in Figure 14b), relative to Chukotka and Alaska (lower abundance of Triassic grains, apart from the Otuk Formation; Figure 15; short-dashed blue arrow in Figure 14b).

A small number of detrital zircon Lu–Hf data were presented previously by Midwinter et al. [33] from the Romulus Member of the Heiberg Formation (sample 11242; n = 22) and the King Christian Formation (sample 11270; n = 2; the King Christian Formation is correlated with the Remus Member of the Heiberg Formation in the eastern Sverdrup Basin [172]; Figure 2). These analyses were reported to show a wide range of $\varepsilon Hf_{(t)}$ values from +12 to −17 with no discernible trend [Figure 12a; 33]. Two of these Hf analyses have corresponding U–Pb ages that are >10% discordant and are not discussed further. The remaining analyses overlap well with the data from J1737, with more juvenile grains falling on the positive trend exhibited by Carboniferous to Triassic grains in samples from the Pat

Bay, Hoyle Bay, Heiberg and Sandy Point formations (Figure 12a). Several analyses fall below this trend; such grains are also present in sample J1737 (Figure 12a). Consequently, the lack of apparent trend in the Midwinter et al. [33] dataset is attributed to the low number of analyses undertaken. Including the dataset of Midwinter et al. [33], the positive trend between U–Pb age and $\varepsilon Hf_{(t)}$ values for the Carboniferous to Triassic grains in samples from the Pat Bay, Hoyle Bay, Heiberg, King Christian and Sandy Point formations yields an εHf/Ma slope of ~0.1, which equates to a $^{176}Lu/^{177}Hf$ ratio of approximately −0.12 (Figure 12a). This is too steep to be consistent with the radiogenic in-growth of ^{176}Hf within a closed continental crustal reservoir ($^{176}Lu/^{177}Hf$ = 0.015 arrow in Figure 12a) or the reworking of hafnium from zircon in a closed system ($^{176}Lu/^{177}Hf$ = 0 arrow in Figure 12a). It instead requires the progressive addition of older, more radiogenically enriched (i.e., evolved) crustal material into an initially juvenile melt, although temporal changes in the composition of the continental crust sampled could also contribute. Such a trend could feasibly occur in convergent to collisional tectonic settings and has been linked to the local thickening of the continental crust, leading to the transportation of large volumes of old lithospheric crust into the melt generation zone and/or greater crustal contamination as rising magmas traverse increasingly thicker crust [173–175]. The trend of the Hf data could reflect collision between the Siberian craton and the Kara terrane (Severnaya Zemlya and northern Taimyr) during Carboniferous to Permian times [164], or alternatively, diachronous arc accretion and subduction along the eastern margin of Baltica (Famennian to Bashkirian; 316.2–372.3 Ma), followed by the onset of the Uralian Orogeny (Bashkirian onwards; [176]).

Midwinter et al. [33] interpreted their hafnium data to support that Permian to Triassic zircons in the Heiberg and King Christian formations shared a source with detrital zircons of the Devonian clastic wedge and were related to crustal rocks within the AACM. This interpretation assumed that the grains were derived from crustal melts with a present-day $^{176}Lu/^{177}Hf$ value of 0.0093. As argued above, however, these grains were not derived solely from crustal melts and thus this interpretation is untenable. Comparing the new hafnium isotope dataset to published datasets from basement rocks is fraught with uncertainty because whilst the data support mixing between magmatic sources, the composition of evolved crust and the relative proportions of mixing are unconstrained.

5.4. Latest Triassic to Middle Jurassic Sediment Supply on Both Basin Margins

Samples from the Fosheim Member of the Heiberg Formation at Slidre Fiord are compositionally mature, have ultrastable heavy mineral assemblages and detrital zircon age spectra dominated by *c*. 950–2100 Ma ages (Figures 3, 5 and 10). This is in stark contrast to the underlying Romulus Member sands. The available data support a recycled sourced from Silurian to Devonian strata of the Franklinian Basin succession, similar to the Carboniferous to Middle Triassic sands on the southern margin (Section 5.1). This is consistent with previous studies that have inferred a provenance from the south and/or east for the Fosheim Member [16,18–20,86]. The multi-proxy dataset presented herein conclusively and unambiguously shows that the Romulus and Fosheim members are genetically unrelated.

Probable Heiberg Formation samples from Lake Hazen (S_HS0292 and S_HS0520), as well as samples from the Heiberg or Sandy Point formations (S_HS0353 and S_HS0368), and samples from the undifferentiated Heiberg Formation in the Sawtooth Range also have heavy mineral assemblages largely dominated by ultrastable minerals (zircon, tourmaline and rutile) and zircon age spectra characterised by *c*. 950–2100 Ma grains (Figures 5 and 9). Palaeocurrent indicators measured from one of the sampled sections in the Sawtooth Range indicate flow predominantly towards the west, northwest and north. These data collectively support a similar source from the Franklinian Basin succession to the south/southeast. Nearly all of the undifferentiated Heiberg Formation samples from the Sawtooth Range additionally contain non-trivial amounts of garnet, which is sporadically accompanied by staurolite and chloritoid (Figure 5). The limited heavy mineral yield from sample

S_PH0011 (Schei Point Group) suggests that garnet-bearing detritus was also supplied to this area during Middle to early Late Triassic times. The rutile trace element data from sample S_HS0353 also indicate a detrital contribution from higher-grade, granulite-facies metapelitic rocks (Figure 8) during the deposition of the upper Heiberg or Sandy Point formations in the Lake Hazen area. These minerals indicate a detrital contribution from metasedimentary rocks as well as sedimentary rocks. The garnet grains analysed from sample D4512 suggest a greater input from a granulite-facies metamorphic terrain for the first time. It is, however, unclear whether these garnets reflect the northern and/or southern source area, or indeed whether they are recycled. Such detritus could be recycled from Neoproterozoic to Cambrian strata within the Franklinian Basin succession, which were derived from the Canadian-Greenland Shield [42,49], or sourced from the shield itself. Neoproterozoic to Cambrian strata of the Franklinian Basin have yielded distinctive detrital zircon age spectra characterised by large *c.* 1750–2000 and 2500–3000 Ma age groups (Figure 9). These age groups are not apparent in the Sverdrup Basin samples, which may suggest that the detrital contribution from this source was not sufficiently large or zircon-rich to affect their detrital zircon age spectra.

Sandy Point Formation samples from northern Axel Heiberg Island and Slidre Fiord are compositionally mature (C403747) to immature (D4542, D4544), apatite-rich, and contain both plagioclase and Carboniferous to Triassic detrital zircons (Figures 3–5 and 10). These samples, however, contain few near syn-depositional detrital zircons. One grain from sample D4542 analysed using LA-ICPMS yielded a near syn-depositional Jurassic age (180.1 ± 3.5 Ma; 2s, concordia age), although, as noted in Section 4.6, subsequent SIMS analyses failed to identify similar-aged grains. Conversely, a single Pliensbachian-aged grain was reported from sample C403747 by Omma et al. ([34]; 186.8 ± 4.8 Ma; 2s, concordia age). All other analyses from these samples (n = 208) yield Late Triassic (207 Ma) and older ages. Consequently, the two apparent Jurassic grains may have suffered some radiogenic lead loss. These data support previous suggestions that Jurassic and younger sediments deposited on the northern flank of the basin contain few or no syn-depositional aged detrital zircons [33,36]. Carboniferous to Triassic detrital zircons in samples C403747 and D4542 yield the same $\varepsilon Hf_{(t)}$ ranges as grains in sample J1737 from the Romulus Member of the Heiberg Formation (Figure 12a). Sandy Point Formation samples from Slidre Fiord contain less apatite, have lower ATi values and higher ZTR values (Figure 5) than the majority of samples from the local Romulus Member. All of this suggests that local Late Triassic strata were a major source for these Sandy Point Formation samples. The strata on northern Axel Heiberg Island were derived from the north based on sedimentary facies spatial trends [17,23]. The northern basin margin is interpreted to have undergone uplift during Middle Jurassic times and developed into a rift-flank shoulder (Sverdrup Rim) in response to rifting in the adjacent proto-Amerasia Basin [19,23,27]. This uplift is inferred to have facilitated the erosion and recycling of local Late Triassic strata, leading to their redeposition in the Sandy Point Formation.

5.5. Triassic to Jurassic Regional Palaeogeographic Implications

The available data suggest that northern-derived Middle Permian to Early Triassic sediments deposited on the northern flank of the Sverdrup Basin are genetically unrelated to Late Triassic ones. As argued in Section 5.2, Middle Permian to Early Triassic sediments were likely derived from land to the north of the Sverdrup Basin. Based on the available detrital zircon U–Pb and Lu–Hf data these sediments were sourced from an area that included juvenile Timanian crust. This was likely the Chukotkan part of the AACM, which is inferred as lying proximal to the eastern part of the Sverdrup Basin (Figure 14a; e.g., [7]). Input into the eastern Sverdrup Basin from the north gradually waned during Early Triassic times [17]. The New Siberian Islands, Chukotka and Wrangel Island experienced active rifting during the latest Permian to Early Triassic [8–10]. This is evidenced by voluminous gabbroic dykes and sills at the base of the Triassic section in Chukotka [10], which have yielded a U–Pb zircon concordia age of 252 ± 4 Ma [177,178]. Subvolcanic intrusions on

the New Siberian Islands have yielded an indistinguishable U–Pb zircon concordia age of 252 ± 2 Ma [179]. These intrusions have similar chemistry and are coeval with the Siberian Traps, suggesting that this part of the AACM was proximal to Siberia during Triassic times [7]. We speculate that rifting in the Chukotkan part of the AACM may have caused the area of the microplate adjacent to the eastern Sverdrup Basin to founder and no longer provide sediment, and that this may account for the loss of northern-derived sediment input into the eastern Sverdrup Basin during Early Triassic times. Sediment supply from Crockerland is inferred to have continued in the western Sverdrup Basin during the deposition of the Carnian Pat Bay Formation [32]. As explained in Section 5.3, Late Triassic strata from the eastern Sverdrup Basin, Barents Shelf, Svalbard, Franz Josef Land, Alaska, St Lawrence Island, Chukotka and Wrangel Island have very similar detrital zircon age spectra, supporting a common Uralian orogenic belt/Arctic Uralides provenance. It has been suggested that Crockerland formed a low-lying land bridge during Late Triassic times, carrying sediment from this orogenic belt to the various aforementioned areas of the Arctic [32,180]. However, the body of evidence that supports northwestward sediment supply across the Barents Shelf and overspilling into the Sverdrup Basin [78,147] makes the land bridge superfluous. Furthermore, the land bridge is incompatible with the shallow to deepwater environments that characterised much of the Chukotkan part of the AACM during this time (e.g., [8,10,151]). Instead, the dispersal of such sands to the various distant areas of the Arctic implies that Crockerland was no longer a topographic/bathymetric obstacle and thus was greatly diminished in size (Figure 14b), or non-existant [171] by this time. It is noteworthy that sands bearing similar detrital zircon age spectra have not been reported from the North Alaskan margin (Figure 14b; [11]). Whether this is a function of distance from the Uralian orogenic belt or a topographic/bathymetric shadowing effect generated by a residual Crockerland proximal to the western Sverdrup Basin is unclear. If a vestigial Crockerland still existed by this time it may speculatively suggest that Early Triassic rifting within the Chukotkan part of the AACM did not propagate into the Alaskan part. This is supported by the stratigraphic record of northern Alaska which is characterized by a relatively thin, clastic passive margin succession, which includes chert and other pelagic deposits in the south and more proximal thin platform sandstones in the north [10].

The loss of northern-derived sand input into the Sverdrup Basin has been suggested to be related to rifting in the proto-Amerasia Basin leading to dismembering of the source area and the trapping of northern-derived sediment within intervening extensional grabens [17–19,23,29,33,36]. Using detrital zircon U–Pb age data, Midwinter et al. [33] constrained this to have occurred after the deposition of the Romulus Member and before the deposition of the King Christian Formation (the western equivalent to the Remus Member of the Heiberg Formation in the eastern part of the Sverdrup Basin; [172]). Narrow rift sub-basins developed along the western margin of the Sverdrup Basin in the Prince Patrick Island area are linked with rifting in the adjacent Amerasia Basin [19,181]. The inferred presence of upper Heiberg Group strata in these sub-basins [181] has been used to further support the onset of rifting during latest Triassic to Sinemurian times [33,36]. However, no wells penetrate these strata and the authors of the original work inferred a later, Toarcian to Aalenian onset for rifting [181]. Moreover, the oldest strata known from the nearby Banks Basin are Middle to Late Jurassic in age [20,182]. Accepting that Late Triassic sands within the Sverdrup Basin are derived from the Uralian Orogen/Arctic Uralides via the Barents Shelf, then it is possible that the loss of this sand input from the Sverdrup Basin record reflects drainage reorganisation on the Barents Shelf. The timing of the disappearance of Uralian-derived sands on the southwest Barents Shelf is contentious, with estimates varying between early Norian and Sinemurian times [154–158,183]. However, the development of a forebulge and associated basins has been suggested as the probable cause [155,158,183]. This likely restricted sediment overspill from the Barents Shelf and may account for the loss of Late Triassic, inferred Uralian-derived sands within the Sverdrup Basin. Conversely, late Toarcian to Aalenian sandstones of the Sandy Point Formation deposited on northern Axel Heiberg Island and at Slidre Fiord were likely recycled from local Triassic strata to the

north of the basin. We speculate that this was facilitated by rift-flank uplift of the northern Sverdrup Basin margin related to rifting in the proto-Amerasia Basin to the north.

6. Conclusions

A multi-proxy provenance study of Late Carboniferous to Middle Jurassic siliciclastic sediments in the eastern Sverdrup Basin was undertaken, employing optical petrography, heavy mineral analysis, single-grain mineral chemistry, detrital zircon U–Pb geochronology and detrital zircon Lu–Hf isotope analysis. Late Carboniferous to Middle Jurassic strata on the southern margin of the basin are inferred as being reworked from local Franklinian Basin succession. Climate-driven compositional variations are apparent within the Late Carboniferous to Early Triassic stratigraphic interval. Higher-grade metamorphic detritus appears in Middle to Late Triassic strata in the vicinity of the Sawtooth Range, Fosheim Peninsula, Ellesmere Island. This may indicate exhumation and erosion of lower levels within the Franklinian Basin succession or direct input from the Canadian-Greenland Shield. Northern-derived Middle Permian to Early Triassic sediments deposited on the northern flank of the basin were sourced from an area comprising Franklinian Basin strata and juvenile crust consistent with the Timanide Orogen. These sediments were likely sourced from proximal areas of the Chukotkan portion of the AACM, which formed part of Crockerland, and lay adjacent to the eastern Sverdrup Basin at this time. Late Triassic northern-derived sediments are compositionally distinct from Middle Permian to Early Triassic ones and were derived from the Uralian orogenic belt and/or its Arctic Uralides extension. The loss of this sand supply during latest Triassic times is interpreted to reflect drainage reorganisation farther upstream on the Barents Shelf. The data obtained from Middle Jurassic sands in the northern and axial regions of the eastern Sverdrup Basin are consistent with the reworking and redeposition of local northern-derived Late Triassic strata. These sediments were supplied from the north, possibly through rift flank uplift of the northern basin margin area in response to rifting in the proto-Amerasia Basin.

Supplementary Materials: The following are available online at https://www.mdpi.com/article/10.3390/geosciences13010010/s1, File S1: Analytical Methods, Table S1: A list of the samples studied and the analyses undertaken, Table S2: Optical petrography dataset, Table S3: Conventional heavy mineral data, Table S4: Apatite trace element data, Table S5: Garnet major element data, Table S6: Rutile trace element data, Table S7: Detrital zircon U-Pb isotope data, Table S8: Detrital zircon Lu-Hf isotope data.

Author Contributions: Conceptualization, H.S., J.E.O., R.A.S., M.A.P., M.J.F. and A.C.M.; Methodology, A.C.M., D.F., I.M., M.J.W. and Q.G.C.; Formal Analysis, M.A.P., H.S., J.E.O., M.J.F., A.C.M., S.J.R. and B.L.-M.; Investigation, A.C.M., H.S., J.E.O., M.A.P., M.J.F., I.M., Q.G.C., S.S., P.H., S.J.R. and D.F.; Data curation, M.A.P., H.S., J.E.O., A.C.M., S.J.R. and B.L.-M.; Writing—Original Draft Preparation, M.A.P.; Writing—Review and Editing, J.E.O., M.J.F., S.S., A.C.M., B.L.-M., S.J.R., Q.G.C., M.J.W. and I.M.; Visualization, M.A.P. and S.S.; Project Administration and Supervision, H.S., R.A.S., M.J.F. and P.H. All authors have read and agreed to the published version of the manuscript.

Funding: This research received no external funding.

Data Availability Statement: The data presented in this study are available in the supplementary materials.

Acknowledgments: This research was funded by CASP's industrial sponsors. Ashton Embry is kindly acknowledged for providing some of the samples used in this study. We are grateful to several people who helped with the collection of data presented herein. This includes Andy Carter (University College London) and Joe Petrus (formerly Laurentian University, now Elemental Scientific Lasers) and Iain McDonald (Cardiff University). Balz Kamber (Queensland University of Technology) is also acknowledged for facilitating access to the ICP facility at Laurentian University. Thoughtful and constructive comments from two anonymous reviewers have improved this manuscript and are gratefully acknowledged.

Conflicts of Interest: The authors declare no conflict of interest.

References

1. Coakley, B.; Brumley, K.; Lebedeva-Ivanova, N.; Mosher, D. Exploring the geology of the central Arctic Ocean; understanding the basin features in place and time. *J. Geol. Soc.* **2016**, *173*, 967–987. [CrossRef]
2. Døssing, A.; Jackson, H.R.; Matzka, J.; Einarsson, I.; Rasmussen, T.M.; Olesen, A.V.; Brozena, J.M. On the origin of the Amerasia Basin and the High Arctic Large Igneous Province—Results of new aeromagnetic data. *Earth Planet. Sci. Lett.* **2013**, *363*, 219–230. [CrossRef]
3. Grantz, A.; Hart, P.E.; Childers, V.A. Geology and tectonic development of the Amerasia and Canada Basins, Arctic Ocean. *Geol. Soc. Lond. Mem.* **2011**, *35*, 771–799. [CrossRef]
4. Lawver, L.A.; Scotese, C.R. A review of tectonic models for the evolution of the Canada Basin. *Geol. N. Am.* **1990**, *50*, 593–618.
5. Nikishin, A.M.; Petrov, E.I.; Cloetingh, S.; Freiman, S.I.; Malyshev, N.A.; Morozov, A.F.; Posamentier, H.W.; Verzhbitsky, V.E.; Zhukov, N.N.; Startseva, K. Arctic Ocean Mega Project: Paper 3—Mesozoic to Cenozoic geological evolution. *Earth Sci. Rev.* **2021**, *217*, 103034. [CrossRef]
6. Pease, V.; Drachev, S.; Stephenson, R.; Zhang, X. Arctic lithosphere—A review. *Tectonophysics* **2014**, *628*, 1–25. [CrossRef]
7. Miller, E.L.; Meisling, K.E.; Akinin, V.V.; Brumley, K.; Coakley, B.J.; Gottlieb, E.S.; Hoiland, C.W.; O'Brien, T.M.; Soboleva, A.; Toro, J. Circum-Arctic Lithosphere Evolution (CALE) Transect C: Displacement of the Arctic Alaska–Chukotka microplate towards the Pacific during opening of the Amerasia Basin of the Arctic. *Geol. Soc. Spec. Publ.* **2018**, *460*, 57–120. [CrossRef]
8. Miller, E.L.; Gehrels, G.E.; Pease, V.; Sokolov, S. Stratigraphy and U-Pb detrital zircon geochronology of Wrangel Island, Russia: Implications for Arctic paleogeography. *AAPG Bull.* **2010**, *94*, 665–692. [CrossRef]
9. Miller, E.L.; Soloviev, A.V.; Prokopiev, A.V.; Toro, J.; Harris, D.; Kuzmichev, A.B.; Gehrels, G.E. Triassic river systems and the paleo-Pacific margin of northwestern Pangea. *Gondwana Res.* **2013**, *23*, 1631–1645. [CrossRef]
10. Miller, E.L.; Toro, J.; Gehrels, G.; Amato, J.M.; Prokopiev, A.; Tuchkova, M.I.; Akinin, V.V.; Dumitru, T.A.; Moore, T.E.; Cecile, M.P. New insights into Arctic paleogeography and tectonics from U-Pb detrital zircon geochronology. *Tectonics* **2006**, *25*, TC3013. [CrossRef]
11. Gottlieb, E.S.; Meisling, K.E.; Miller, E.L.; Mull, C.G.G. Closing the Canada Basin: Detrital zircon geochronology relationships between the North Slope of Arctic Alaska and the Franklinian mobile belt of Arctic Canada. *Geosphere* **2014**, *10*, 1366–1384. [CrossRef]
12. Pease, V.L.; Kuzmichev, A.B.; Danukalova, M.K. The New Siberian Islands and evidence for the continuation of the Uralides, Arctic Russia. *J. Geol. Soc.* **2015**, *172*, 1–4. [CrossRef]
13. Ershova, V.B.; Khudoley, A.K.; Prokopiev, A.V.; Tuchkova, M.I.; Fedorov, P.V.; Kazakova, G.G.; Shishlov, S.B.; O'Sullivan, P. Trans-Siberian Permian rivers: A key to understanding Arctic sedimentary provenance. *Tectonophysics* **2016**, *691*, 220–233. [CrossRef]
14. Ershova, V.B.; Lorenz, H.; Prokopiev, A.V.; Sobolev, N.N.; Khudoley, A.K.; Petrov, E.O.; Estrada, S.; Sergeev, S.; Larionov, A.; Thomsen, T.B. The De Long Islands: A missing link in unraveling the Paleozoic paleogeography of the Arctic. *Gondwana Res.* **2016**, *35*, 305–322. [CrossRef]
15. Alonso-Torres, D.; Beauchamp, B.; Guest, B.; Hadlari, T.; Matthews, W. Late Paleozoic to Triassic arc magmatism north of the Sverdrup Basin in the Canadian Arctic: Evidence from detrital zircon U-Pb geochronology. *Lithosphere* **2018**, *10*, 426–445. [CrossRef]
16. Balkwill, H.R. Evolution of Sverdrup Basin, Arctic Canada. *AAPG Bull.* **1978**, *62*, 1004–1028.
17. Embry, A.F. Crockerland—The Source Area for the Triassic to Middle Jurassic Strata of Northern Axel Heiberg Island, Canadian Arctic Islands. *Bull. Can. Pet. Geol.* **2009**, *57*, 129–140. [CrossRef]
18. Embry, A.F.; Beauchamp, B. Sverdrup Basin. In *The Sedimentary Basins of the United States and Canada*, 2nd ed.; Miall, A.D., Ed.; Elsevier: Amsterdam, The Netherlands, 2019; pp. 559–592.
19. Embry, A.F.; Beauchamp, B. Sverdrup Basin. In *The Sedimentary Basins of the United States and Canada*, 1st ed.; Miall, A.D., Ed.; Elsevier: Amsterdam, The Netherlands, 2008; pp. 451–471.
20. Embry, A.F. Mesozoic History of the Arctic Islands. In *Geology of the Innuitian Orogen and Arctic Platform of Canada and Greenland. Geology of Canada no. 3*; Trettin, H.P., Ed.; Geological Survey of Canada: Ottawa, ON, Canada, 1991; pp. 371–433.
21. Smyth, H.R.; Morton, A.; Scott, R.A.; Omma, J.E.; Kelly, S.R.; Rippington, S.; Braham, B.; Gregory, U.J.; Jolley, D. Evolution of the Sverdrup Basin: New insights from field studies, integrated biostratigraphy & sediment provenance analyses. In Proceedings of the GeoCanada 2010—Working with the Earth, Calgary, AB, Canada, 10–14 May 2010; pp. 1–4.
22. Patchett, P.J.; Embry, A.F.; Ross, G.M.; Beauchamp, B.; Harrison, J.C.; Mayr, U.; Isachsen, C.E.; Rosenberg, E.J.; Spence, G.O. Sedimentary Cover of the Canadian Shield through Mesozoic Time Reflected by Nd Isotopic and Geochemical Results for the Sverdrup Basin, Arctic Canada. *J. Geol.* **2004**, *112*, 39–57. [CrossRef]
23. Embry, A.F. Crockerland—The northwest source area for the Sverdrup Basin, Canadian Arctic Islands. In *Arctic Geology and Petroleum Potential*; Vorren, T.O., Bergsager, E., Dahl-Stamnes, Ø.A., Holter, E., Johansen, B., Lie, E., Lund, T.B., Eds.; Elsevier: Amsterdam, The Netherlands, 1993; Volume 2, pp. 205–216.
24. Laverov, N.P.; Lobkovsky, L.I.; Kononov, M.V.; Dobretsov, N.L.; Vernikovsky, V.A.; Sokolov, S.D.; Shipilov, E.V. A geodynamic model of the evolution of the Arctic basin and adjacent territories in the Mesozoic and Cenozoic and the outer limit of the Russian Continental Shelf. *Geotectonics* **2013**, *47*, 1–30. [CrossRef]

25. Zonenshain, L.P.; Natapov, L.M. Tectonic History of the Arctic Region from the Ordovician Through the Cretaceous. In *The Arctic Seas: Climatology, Oceanography, Geology, and Biology*; Herman, Y., Ed.; Springer: Boston, MA, USA, 1989; pp. 829–862.
26. Embry, A.F. Geological and geophysical evidence in support of the hypothesis of anticlockwise rotation of northern Alaska. *Mar. Geol.* **1990**, *93*, 317–329. [CrossRef]
27. Embry, A.F.; Dixon, J. The age of the Amerasia Basin. In Proceedings of the 1992 International Conference on Arctic Margins, Anchorage, AK, USA, 2–4 September 1992; pp. 289–295.
28. Grantz, A.; May, S.D.; Hart, P.E. Geology of the Arctic Continental Margin of Alaska. In *The Arctic Ocean Region*; Grantz, A., Johnson, L., Sweeney, J.F., Eds.; Geological Society of America: Boulder, CO, USA, 1990; Volume L, pp. 257–288.
29. Embry, A.F.; Anfinson, O.A. A History of Crockerland—The Little Arctic Terrane that Could. In Proceedings of the GeoConvention 2013: Integration, Calgary, AB, Canada, 6–12 May 2013; pp. 1–4.
30. Hadlari, T.; Dewing, K.; Matthews, W.A.; Alonso-Torres, D.; Midwinter, D. Early Triassic development of a foreland basin in the Canadian high Arctic: Implications for a Pangean Rim of Fire. *Tectonophysics* **2018**, *736*, 75–84. [CrossRef]
31. Galloway, B.J.; Dewing, K.; Beauchamp, B.; Matthews, W. Upper Paleozoic stratigraphy and detrital zircon geochronology along the northwest margin of the Sverdrup Basin, Arctic Canada: Insight into the paleogeographic and tectonic evolution of Crockerland. *Can. J. Earth Sci.* **2021**, *58*, 164–187. [CrossRef]
32. Anfinson, O.A.; Embry, A.F.; Stockli, D.F. Geochronologic Constraints on the Permian–Triassic Northern Source Region of the Sverdrup Basin, Canadian Arctic Islands. *Tectonophysics* **2016**, *691*, 206–219. [CrossRef]
33. Midwinter, D.; Hadlari, T.; Davis, W.J.; Dewing, K.; Arnott, R.W.C. Dual provenance signatures of the Triassic northern Laurentian margin from detrital-zircon U-Pb and Hf-isotope analysis of Triassic–Jurassic strata in the Sverdrup Basin. *Lithosphere* **2016**, *8*, 668–683. [CrossRef]
34. Omma, J.E.; Pease, V.; Scott, R.A. U–Pb SIMS zircon geochronology of Triassic and Jurassic sandstones on northwestern Axel Heiberg Island, northern Sverdrup Basin, Arctic Canada. *Geol. Soc. Lond. Mem.* **2011**, *35*, 559–566. [CrossRef]
35. Pease, V. Eurasian orogens and Arctic tectonics: An overview. *Geol. Soc. Lond. Mem.* **2011**, *35*, 311–324. [CrossRef]
36. Hadlari, T.; Midwinter, D.; Galloway, J.M.; Dewing, K.; Durbano, A.M. Mesozoic rift to post-rift tectonostratigraphy of the Sverdrup Basin, Canadian Arctic. *Mar. Pet. Geol.* **2016**, *76*, 148–158. [CrossRef]
37. Jakobsson, M.; Mayer, L.A.; Bringensparr, C.; Castro, C.F.; Mohammad, R.; Johnson, P.; Ketter, T.; Accettella, D.; Amblas, D.; An, L.; et al. The International Bathymetric Chart of the Arctic Ocean Version 4.0. *Sci. Data* **2020**, *7*, 176. [CrossRef]
38. Harrison, J.; St-Onge, M.; Petrov, O.; Strelnikov, S.; Lopatin, B.; Wilson, F.; Tella, S.; Paul, D.; Lynds, T.; Shokalsky, S. *Geological Map of the Arctic. Map 2159A*; Geological Survey of Canada: Ottawa, ON, Canada, 2011.
39. St-Onge, M.R.; Van Gool, J.A.M.; Garde, A.A.; Scott, D.J. Correlation of Archaean and Palaeoproterozoic units between northeastern Canada and western Greenland: Constraining the pre-collisional upper plate accretionary history of the Trans-Hudson orogen. *Geol. Soc. Spec. Publ.* **2009**, *318*, 193–235. [CrossRef]
40. Frisch, T. *Reconnaissance Geology of the Precambrian Shield of Ellesmere, Devon and Coburg Islands, Arctic Archipelago: A Preliminary Account*; Geological Survey of Canada Paper; Geological Survey of Canada: Ottawa, ON, Canada, 1983; Volume 82-10, pp. 1–11.
41. Frisch, T.; Hunt, P.A. U-Pb zircon and motzcizite ages from the Precambrian Shield of Ellesmere and Devon islands, Artic Archipelago. In *U-Pb Zircon and Motzcizite Ages from the Precambrian Shield of Ellesmere and Devon islands, Artic Archipelago. Radiogenic Age and Isotopic Studies: Report 2*; Geological Survey of Canada Paper; Geological Survey of Canada: Ottawa, ON, Canada, 1988; Volume 88-2, pp. 117–125.
42. Anfinson, O.A.; Leier, A.L.; Embry, A.F.; Dewing, K. Detrital zircon geochronology and provenance of the Neoproterozoic to Late Devonian Franklinian Basin, Canadian Arctic Islands. *Geol. Soc. Am. Bull.* **2012**, *124*, 415–430. [CrossRef]
43. Anfinson, O.A.; Leier, A.L.; Gaschnig, R.; Embry, A.F.; Dewing, K.; Colpron, M. U–Pb and Hf isotopic data from Franklinian Basin strata: Insights into the nature of Crockerland and the timing of accretion, Canadian Arctic Islands. *Can. J. Earth Sci.* **2012**, *49*, 1316–1328. [CrossRef]
44. Thorsteinsson, R.; Tozer, E. *Summary Account of Structural History of the Canadian Arctic Archipelago since Precambrian Time*; Geological Survey of Canada Paper; Geological Survey of Canada: Ottawa, ON, Canada, 1960; Volume 60–67, pp. 1–25.
45. Thorsteinsson, R.; Tozer, E. Geology of the Arctic archipelago. In *Geology and Economic Minerals of Canada*; Douglas, R.J.W., Ed.; Department of Energy, Mines and Resources: Ottawa, ON, Canada, 1970; Volume 1, pp. 547–590.
46. Trettin, H.P.; Mayr, U.; Long, G.D.F.; Packard, J.J. Cambrian to Early Devonian Basin Development, Sedimentation, and Volcanism, Arctic Islands. Geology of Canada no. 3. In *Geology of the Innuitian Orogen and Arctic Platform of Canada and Greenland*; Trettin, H.P., Ed.; Geological Survey of Canada: Ottawa, ON, Canada, 1991; pp. 165–238.
47. Beranek, L.P.; Pease, V.; Scott, R.A.; Thomsen, T.B.; Mahoney, J.B. Detrital zircon geochronology of Ediacaran to Cambrian deep-water strata of the Franklinian basin, northern Ellesmere Island, Nunavut: Implications for regional stratigraphic correlations. *Can. J. Earth Sci.* **2013**, *50*, 1007–1018. [CrossRef]
48. Dewing, K.; Harrison, J.C.; Pratt, B.R.; Mayr, U. A probable late Neoproterozoic age for the Kennedy Channel and Ella Bay formations, northeastern Ellesmere Island and its implications for passive margin history of the Canadian Arctic. *Can. J. Earth Sci.* **2004**, *41*, 1013–1025. [CrossRef]
49. Patchett, P.J.; Roth, M.A.; Canale, B.S.; de Freitas, T.A.; Harrison, J.C.; Embry, A.F.; Ross, G.M. Nd isotopes, geochemistry, and constraints on sources of sediments in the Franklinian mobile belt, Arctic Canada. *GSA Bull.* **1999**, *111*, 578–589. [CrossRef]

50. Malone, S.J.; McClelland, W.C.; Gosen, W.v.; Piepjohn, K. Detrital zircon U-Pb and Lu-Hf analysis of Paleozoic sedimentary rocks from the Pearya terrane and Ellesmerian Fold Belt (northern Ellesmere Island): A comparison with Circum-Arctic datasets and their implications on terrane tectonics. *Geol. Soc. Am. Spec. Pap.* **2018**, *541*, 231–254.
51. Trettin, H.P. Pearya: A composite terrane with Caledonian affinities in northern Ellesmere Island. *Can. J. Earth Sci.* **1987**, *24*, 224–245. [CrossRef]
52. Trettin, H.P. The Proterozoic to Late Silurian Record of Pearya. In *Geology of the Innuitian Orogen and Arctic Platform of Canada and Greenland. Geology of Canada no.3*; Trettin, H.P., Ed.; Geological Survey of Canada: Ottawa, ON, Canada, 1991; pp. 241–260.
53. Dewing, K.; Hadlari, T.; Pearson, D.G.; Matthews, W. Early Ordovician to Early Devonian tectonic development of the northern margin of Laurentia, Canadian Arctic Islands. *GSA Bull.* **2019**, *131*, 1075–1094. [CrossRef]
54. Malone, S.J.; McClelland, W.C.; von Gosen, W.; Piepjohn, K. Proterozoic Evolution of the North Atlantic–Arctic Caledonides: Insights from Detrital Zircon Analysis of Metasedimentary Rocks from the Pearya Terrane, Canadian High Arctic. *J. Geol.* **2014**, *122*, 623–647. [CrossRef]
55. Malone, S.J.; McClelland, W.C.; von Gosen, W.; Piepjohn, K. The earliest Neoproterozoic magmatic record of the Pearya terrane, Canadian high Arctic: Implications for Caledonian terrane reconstructions. *Precambrian Res.* **2017**, *292*, 323–349. [CrossRef]
56. Trettin, H.P.; Parrish, R.; Roddick, J. New U-Pb and 40Ar-39Ar age determinations from northern Ellesmere and Axel Heiberg Islands and their tectonic significance. In *Radiogenic Age and Isotopic Studies: Report 6*; Geological Survey of Canada Paper; Geological Survey of Canada: Ottawa, ON, Canada, 1992; Volume 92-2, pp. 3–30.
57. Hadlari, T.; Davis, W.J.; Dewing, K. A pericratonic model for the Pearya terrane as an extension of the Franklinian margin of Laurentia, Canadian Arctic. *Geol. Soc. Am. Bull.* **2014**, *126*, 182–200. [CrossRef]
58. Beranek, L.P.; Pease, V.; Hadlari, T.; Dewing, K. Silurian flysch successions of Ellesmere Island, Arctic Canada, and their significance to northern Caledonian palaeogeography and tectonics. *J. Geol. Soc.* **2015**, *172*, 201–212. [CrossRef]
59. Embry, A.F. Middle-Upper Devonian Clastic Wedge of the Arctic Islands. In *Geology of the Innuitian Orogen and Arctic Platform of Canada and Greenland. Geology of Canada no. 3*; Trettin, H.P., Ed.; Geological Survey of Canada: Ottawa, ON, Canada, 1991; pp. 263–280.
60. Embry, A.F.; Klovan, J.E. The Middle-Upper Devonian clastic wedge of the Franklinian geosyncline. *Bull. Can. Pet. Geol.* **1976**, *24*, 485–639.
61. Embry, A.F. Middle-Upper Devonian sedimentation in the Canadian Arctic Islands and the Ellesmerian Orogeny. In *Devonian of the World: Proceedings of the 2nd International Symposium on the Devonian System—Volume II: Sedimentation*; McMillan, N.J., Embry, A.F., Glass, D.J., Eds.; Canadian Society of Petroleum Geologists: Calgary, AB, Canada, 1988; Volume 14, pp. 15–28.
62. Beauchamp, B. Carboniferous and Permian subsurface stratigraphy, Prince Patrick Island, Northwest Territories, Canadian Arctic. *Geol. Surv. Can. Bull.* **2001**, *565*, 1–96.
63. Davies, G.R.; Nassichuk, W.W. Carboniferous and Permian History of the Sverdrup Basin, Arctic Islands. In *Geology of the Innuitian Orogen and Arctic Platform of Canada and Greenland. Geology of Canada no. 3*; Trettin, H.P., Ed.; Geological Survey of Canada: Ottawa, ON, Canada, 1991; pp. 345–367.
64. Trettin, H.P. Early Namurian (or older) alkali basalt in the Borup Fiord Formation, northern Axel Heiberg Island, Arctic Canada. In *Current Research, Part D, Interior Plains and Arctic Canada*; Geological Survey of Canada Paper; Geological Survey of Canada: Ottawa, ON, Canada, 1988; Volume 88-1D, pp. 21–26.
65. Nassichuk, W.W.; Davies, G.R. Stratigraphy and Sedimentation of the Otto Fiord Formation-a Major Mississippian Pennsylvanian Evaporite of Subaqueous Origin in the Canadian Arctic Archipelago. *Geol. Surv. Can. Bull.* **1980**, *286*, 1–87.
66. Cameron, B.I.; Muecke, G.K. Permian alkaline basalts associated with formation of the Sverdrup Basin, Canadian Arctic. *Can. J. Earth Sci.* **1996**, *33*, 1462–1473. [CrossRef]
67. Morris, N. Stratigraphy and Geochemistry of Lower Permian volcanics in the Sverdrup Basin, Northwest Ellesmere Island, Nunavut. Master's Thesis, University of Calgary, Calgary, AB, Canada, 2013.
68. Lopez-Mir, B.; Schneider, S.; Hülse, P. Fault activity and diapirism in the Mississippian to Late Cretaceous Sverdrup Basin: New insights into the tectonic evolution of the Canadian Arctic. *J. Geodyn.* **2018**, *118*, 55–65. [CrossRef]
69. Embry, A.F. The Wilkie Point Group (Lower-Upper Jurassic), Sverdrup Basin, Arctic Islands. In *Current Research, Part B*; Geological Survey of Canada Paper; Geological Survey of Canada: Ottawa, ON, Canada, 1984; Volume 84-1B, pp. 299–308.
70. Cohen, K.M.; Finney, S.C.; Gibbard, P.L.; Fan, J.-X. The ICS international chronostratigraphic chart. *Episodes* **2013**, *36*, 199–204. [CrossRef]
71. Thorsteinsson, R. Carboniferous and Permian stratigraphy of Axel Heiberg Island and western Ellesmere Island, Canadian Arctic Archipelago. *Geol. Surv. Can. Bull.* **1974**, *224*, 1–115.
72. Stephenson, R.; Boerstoel, J.; Embry, A.F.; Ricketts, B.D. Subsidence analysis and tectonic modeling of the Sverdrup Basin. In Proceedings of the 1992 International Conference on Arctic Margins, Anchorage, AK, USA, 2–4 September 1992; pp. 149–154.
73. Embry, A.F. Petroleum prospectivity of the Triassic–Jurassic succession of Sverdrup Basin, Canadian Arctic Archipelago. *Geol. Soc. Lond. Mem.* **2011**, *35*, 545–558. [CrossRef]
74. Boutelier, J.; Cruden, A.; Brent, T.; Stephenson, R. Timing and mechanisms controlling evaporite diapirism on Ellef Ringnes Island, Canadian Arctic Archipelago. *Basin Res.* **2011**, *23*, 478–498. [CrossRef]
75. Harrison, J.C.; Jackson, M.P.A. Exposed evaporite diapirs and minibasins above a canopy in central Sverdrup Basin, Axel Heiberg Island, Arctic Canada. *Basin Res.* **2014**, *26*, 567–596. [CrossRef]

76. Grasby, S.E.; Beauchamp, B.; Bond, D.P.G.; Wignall, P.; Talavera, C.; Galloway, J.M.; Piepjohn, K.; Reinhardt, L.; Blomeier, D. Progressive environmental deterioration in northwestern Pangea leading to the latest Permian extinction. *GSA Bull.* **2015**, *127*, 1331–1347. [CrossRef]
77. Zuchuat, V.; Sleveland, A.R.N.; Twitchett, R.J.; Svensen, H.H.; Turner, H.; Augland, L.E.; Jones, M.T.; Hammer, Ø.; Hauksson, B.T.; Haflidason, H.; et al. A new high-resolution stratigraphic and palaeoenvironmental record spanning the End-Permian Mass Extinction and its aftermath in central Spitsbergen, Svalbard. *Palaeogeogr. Palaeoclimatol. Palaeoecol.* **2020**, *554*, 109732. [CrossRef]
78. Gilmullina, A.; Klausen, T.G.; Doré, A.G.; Rossi, V.M.; Suslova, A.; Eide, C.H. Linking sediment supply variations and tectonic evolution in deep time, source-to-sink systems—The Triassic Greater Barents Sea Basin. *GSA Bull.* **2021**, *134*, 1760–1780. [CrossRef]
79. Thériault, P. Synrift sedimentation in the Upper Carboniferous Canyon Fiord Formation, SW Ellesmere Island, Canadian Arctic. Master's Thesis, University of Ottawa, Ottawa, ON, Canada, 1991.
80. Devaney, J.R. Sedimentological highlights of the lower Triassic Bjorne formation, Ellesmere Island, Arctic Archipelago. In *Current Research, Part B*; Geological Survey of Canada Paper; Geological Survey of Canada: Ottawa, ON, Canada, 1991; Volume 91-1B, pp. 33–40.
81. Embry, A.F. Stratigraphic subdivision of the Blind Fiord and Bjorne formations (Lower Triassic), Sverdrup Basin, Arctic Islands. In *Current Research, Part B*; Geological Survey of Canada Paper; Geological Survey of Canada: Ottawa, ON, Canada, 1986; Volume 86-1B, pp. 329–340.
82. Midwinter, D.; Hadlari, T.; Dewing, K. Lower Triassic river-dominated deltaic successions from the Sverdrup Basin, Canadian Arctic. *Palaeogeogr. Palaeoclimatol. Palaeoecol.* **2017**, *476*, 55–67. [CrossRef]
83. Embry, A.F. The Schei Point and Blaa Mountain Groups (Middle-Upper Triassic), Sverdrup Basin, Canadian Arctic Archipelago. In *Current Research, Part B*; Geological Survey of Canada Paper; Geological Survey of Canada: Ottawa, ON, Canada, 1984; Volume 84-1B, pp. 327–336.
84. Suneby, L.B.; Hills, L.V. Palynological zonation of the Heiberg Formation (Triassic-Jurassic) eastern Sverdrup Basin, Arctic Canada. *Bull. Can. Pet. Geol.* **1988**, *36*, 347–361.
85. Embry, A.F. Stratigraphic subdivision of the Heiberg Formation, eastern and central Sverdrup Basin, Arctic Islands. In *Current Research, Part B*; Geological Survey of Canada Paper; Geological Survey of Canada: Ottawa, ON, Canada, 1983; Volume 83-1B, pp. 205–213.
86. Embry, A.F. The Upper Triassic-Lower Jurassic Heiberg deltaic complex of the Sverdrup Basin. In *Arctic Geology and Geophysics: Proceedings of the Third International Symposium on Arctic Geology*; Embry, A.F., Balkwill, H.R., Eds.; Canadian Society of Petroleum Geologists: Calgary, AB, Canada, 1982; pp. 189–217.
87. Ingersoll, R.V.; Bullard, T.F.; Ford, R.L.; Grimm, J.P.; Pickle, J.D.; Sares, S.W. The effect of grain size on detrital modes: A test of the Gazzi-Dickinson point-counting method. *J. Sediment. Res.* **1984**, *54*, 103–116.
88. Folk, R.L. *Petrology of Sedimentary Rocks*; Hemphill Publishing Company: Austin, TX, USA, 1980.
89. Pettijohn, F.J.; Potter, P.E.; Siever, R. *Sand and Sandstone*; Springer: New York, NY, USA, 1987.
90. Galehouse, J.S. Point counting. In *Procedures in Sedimentary Petrology*; Carver, R.E., Ed.; Wiley Interscience: New York, NY, USA, 1971; pp. 385–407.
91. Morton, A.C.; Hallsworth, C. Identifying provenance-specific features of detrital heavy mineral assemblages in sandstones. *Sediment. Geol.* **1994**, *90*, 241–256. [CrossRef]
92. O'Sullivan, G.; Chew, D.; Kenny, G.; Henrichs, I.; Mulligan, D. The trace element composition of apatite and its application to detrital provenance studies. *Earth Sci. Rev.* **2020**, *201*, 103044. [CrossRef]
93. Meinhold, G.; Anders, B.; Kostopoulos, D.; Reischmann, T. Rutile chemistry and thermometry as provenance indicator: An example from Chios Island, Greece. *Sediment. Geol.* **2008**, *203*, 98–111. [CrossRef]
94. Watson, E.B.; Wark, D.A.; Thomas, J.B. Crystallization thermometers for zircon and rutile. *Contrib. Mineral. Petrol.* **2006**, *151*, 413–433. [CrossRef]
95. Schönig, J.; von Eynatten, H.; Tolosana-Delgado, R.; Meinhold, G. Garnet major-element composition as an indicator of host-rock type: A machine learning approach using the random forest classifier. *Contrib. Mineral. Petrol.* **2021**, *176*, 98. [CrossRef]
96. Ludwig, K.R. On the Treatment of Concordant Uranium-Lead Ages. *Geochim. Cosmochim. Acta* **1998**, *62*, 665–676. [CrossRef]
97. Ludwig, K. *User's Manual for Isoplot 3.75: A Geochronological Toolkit for Microsoft Excel*; Berkeley Geochronology Center: Berkeley, CA, USA, 2012; Number 5; p. 75.
98. Andersen, T.; Kristoffersen, M.; Elburg, M.A. Visualizing, interpreting and comparing detrital zircon age and Hf isotope data in basin analysis—A graphical approach. *Basin Res.* **2017**, *30*, 132–147. [CrossRef]
99. Thomas, R.J.; Spencer, C.; Bushi, A.M.; Baglow, N.; Boniface, N.; de Kock, G.; Horstwood, M.S.A.; Hollick, L.; Jacobs, J.; Kajara, S.; et al. Geochronology of the central Tanzania Craton and its southern and eastern orogenic margins. *Precambrian Res.* **2016**, *277*, 47–67. [CrossRef]
100. Söderlund, U.; Patchett, P.J.; Vervoort, J.D.; Isachsen, C.E. The 176Lu decay constant determined by Lu–Hf and U–Pb isotope systematics of Precambrian mafic intrusions. *Earth Planet. Sci. Lett.* **2004**, *219*, 311–324. [CrossRef]
101. Bouvier, A.; Vervoort, J.D.; Patchett, P.J. The Lu–Hf and Sm–Nd isotopic composition of CHUR: Constraints from unequilibrated chondrites and implications for the bulk composition of terrestrial planets. *Earth Planet. Sci. Lett.* **2008**, *273*, 48–57. [CrossRef]
102. Hamilton, N.E.; Ferry, M. ggtern: Ternary Diagrams Using ggplot2. *J. Stat. Softw. Code Snippets* **2018**, *87*, 1–17. [CrossRef]

103. Vervoort, J.D.; Patchett, P.J.; Blichert-Toft, J.; Albarède, F. Relationships between Lu–Hf and Sm–Nd isotopic systems in the global sedimentary system. *Earth Planet. Sci. Lett.* **1999**, *168*, 79–99. [CrossRef]
104. Røhr, T.S.; Davis, W.; Andersen, T.; Dypvik, H.; Embry, A.F. Detrital zircon characteristics of the Lower Cretaceous Isachsen Formation, Sverdrup Basin: Source constraints from age and Hf isotope data. *Can. J. Earth Sci.* **2010**, *47*, 255–271. [CrossRef]
105. Gottlieb, E.S.; Pease, V.; Miller, E.L.; Akinin, V.V. Neoproterozoic basement history of Wrangel Island and Arctic Chukotka: Integrated insights from zircon U–Pb, O and Hf isotopic studies. *Geol. Soc. Spec. Publ.* **2018**, *460*, 183–206. [CrossRef]
106. Akinin, V.V.; Gottlieb, E.S.; Miller, E.L.; Polzunenkov, G.O.; Stolbov, N.M.; Sobolev, N.N. Age and composition of basement beneath the De Long archipelago, Arctic Russia, based on zircon U–Pb geochronology and O–Hf isotopic systematics from crustal xenoliths in basalts of Zhokhov Island. *Arktos* **2015**, *1*, 9. [CrossRef]
107. Sircombe, K.N. Mountains in the shadows of time: Three-dimensional density distribution mapping of U-Pb isotopic data as a visualization aid for geochronological information in concordia diagrams. *Geochem. Geophys. Geosyst.* **2006**, *7*, Q07013. [CrossRef]
108. Griffin, W.L.; Wang, X.; Jackson, S.E.; Pearson, N.J.; O'Reilly, S.Y.; Xu, X.; Zhou, X. Zircon chemistry and magma mixing, SE China: In-situ analysis of Hf isotopes, Tonglu and Pingtan igneous complexes. *Lithos* **2002**, *61*, 237–269. [CrossRef]
109. Cai, K.; Sun, M.; Xiao, W.; Buslov, M.M.; Yuan, C.; Zhao, G.; Long, X. Zircon U-Pb geochronology and Hf isotopic composition of granitiods in Russian Altai Mountain, Central Asian Orogenic Belt. *Am. J. Sci.* **2014**, *314*, 580. [CrossRef]
110. Cao, R.; Bagas, L.; Chen, B.; Wang, Z.; Gao, Y. Geochronology and petrogenesis of the composite Zuluhong Granite, North Xinjiang Province of China: Implications for the crust-mantle interaction and continental crustal growth in Western Tianshan Orogen. *Lithos* **2021**, *380*, 105837. [CrossRef]
111. Chen, B.; Jahn, B.M.; Tian, W. Evolution of the Solonker suture zone: Constraints from zircon U–Pb ages, Hf isotopic ratios and whole-rock Nd–Sr isotope compositions of subduction- and collision-related magmas and forearc sediments. *J. Asian Earth Sci.* **2009**, *34*, 245–257. [CrossRef]
112. He, Z.-Y.; Klemd, R.; Yan, L.-L.; Zhang, Z.-M. The origin and crustal evolution of microcontinents in the Beishan orogen of the southern Central Asian Orogenic Belt. *Earth Sci. Rev.* **2018**, *185*, 1–14. [CrossRef]
113. Li, G.; Cao, M.; Qin, K.; Hollings, P.; Evans, N.J.; Seitmuratova, E.Y. Petrogenesis of ore-forming and pre/post-ore granitoids from the Kounrad, Borly and Sayak porphyry/skarn Cu deposits, Central Kazakhstan. *Gondwana Res.* **2016**, *37*, 408–425. [CrossRef]
114. Li, S.; Wilde, S.A.; Wang, T.; Xiao, W.; Guo, Q. Latest Early Permian granitic magmatism in southern Inner Mongolia, China: Implications for the tectonic evolution of the southeastern Central Asian Orogenic Belt. *Gondwana Res.* **2016**, *29*, 168–180. [CrossRef]
115. Liu, W.; Pan, X.-F.; Liu, D.-Y.; Chen, Z.-Y. Three-step continental-crust growth from subduction accretion and underplating, through intermediary differentiation, to granitoid production. *Int. J. Earth Sci.* **2009**, *98*, 1413–1439. [CrossRef]
116. Li, S.; Chung, S.-L.; Wilde, S.A.; Wang, T.; Xiao, W.-J.; Guo, Q.-Q. Linking magmatism with collision in an accretionary orogen. *Sci. Rep.* **2016**, *6*, 25751. [CrossRef] [PubMed]
117. Li, S.; Wang, T.; Wilde, S.A.; Tong, Y. Evolution, source and tectonic significance of Early Mesozoic granitoid magmatism in the Central Asian Orogenic Belt (central segment). *Earth Sci. Rev.* **2013**, *126*, 206–234. [CrossRef]
118. Li, S.; Wang, T.; Wilde, S.A.; Tong, Y.; Hong, D.; Guo, Q. Geochronology, petrogenesis and tectonic implications of Triassic granitoids from Beishan, NW China. *Lithos* **2012**, *134*, 123–145. [CrossRef]
119. Muhtar, M.N.; Wu, C.-Z.; Santosh, M.; Lei, R.-X.; Feng, Y.; Yang, T.; Ye, H.; Gu, L.-X. Peraluminous granitoid magmatism from isotopically depleted sources: The case of Jing'erquanbei pluton in Eastern Tianshan, Northwest China. *Geol. J.* **2020**, *55*, 117–132. [CrossRef]
120. Shen, P.; Pan, H.; Cao, C.; Zhong, S.; Li, C. The formation of the Suyunhe large porphyry Mo deposit in the West Junggar terrain, NW China: Zircon U–Pb age, geochemistry and Sr–Nd–Hf isotopic results. *Ore Geol. Rev.* **2017**, *81*, 808–828. [CrossRef]
121. Shen, P.; Pan, H.; Hattori, K.; Cooke, D.R.; Seitmuratova, E. Large Paleozoic and Mesozoic porphyry deposits in the Central Asian Orogenic Belt: Geodynamic settings, magmatic sources, and genetic models. *Gondwana Res.* **2018**, *58*, 161–194. [CrossRef]
122. Shen, P.; Pan, H.; Seitmuratova, E. Petrogenesis of the mineralized granitoids from the Kounrad and Borly porphyry Cu deposits and the East Kounrad porphyry Mo deposit in Kazakhstan: Implication for tectonic evolution and mineralization of the western part of the Central Asian Orogenic Belt. *Lithos* **2017**, *286*, 53–74. [CrossRef]
123. Shi, Y.; Anderson, J.L.; Li, L.; Ding, J.; Liu, C.; Zhang, W.; Shen, C. Zircon ages and Hf isotopic compositions of Permian and Triassic A-type granites from central Inner Mongolia and their significance for late Palaeozoic and early Mesozoic evolution of the Central Asian Orogenic Belt. *Int. Geol. Rev.* **2016**, *58*, 967–982. [CrossRef]
124. Su, B.-X.; Qin, K.-Z.; Sakyi, P.A.; Li, X.-H.; Yang, Y.-H.; Sun, H.; Tang, D.-M.; Liu, P.-P.; Xiao, Q.-H.; Malaviarachchi, S.P.K. U–Pb ages and Hf–O isotopes of zircons from Late Paleozoic mafic–ultramafic units in the southern Central Asian Orogenic Belt: Tectonic implications and evidence for an Early-Permian mantle plume. *Gondwana Res.* **2011**, *20*, 516–531. [CrossRef]
125. Su, B.-X.; Qin, K.-Z.; Sakyi, P.A.; Liu, P.-P.; Tang, D.-M.; Malaviarachchi, S.P.K.; Xiao, Q.-H.; Sun, H.; Dai, Y.-C.; Yan, H. Geochemistry and geochronology of acidic rocks in the Beishan region, NW China: Petrogenesis and tectonic implications. *J. Asian Earth Sci.* **2011**, *41*, 31–43. [CrossRef]
126. Tang, J.; Xu, W.-L.; Wang, F.; Zhao, S.; Wang, W. Early Mesozoic southward subduction history of the Mongol–Okhotsk oceanic plate: Evidence from geochronology and geochemistry of Early Mesozoic intrusive rocks in the Erguna Massif, NE China. *Gondwana Res.* **2016**, *31*, 218–240. [CrossRef]

127. Tong, Y.; Jahn, B.-m.; Wang, T.; Hong, D.-w.; Smith, E.I.; Sun, M.; Gao, J.-f.; Yang, Q.-d.; Huang, W. Permian alkaline granites in the Erenhot–Hegenshan belt, northern Inner Mongolia, China: Model of generation, time of emplacement and regional tectonic significance. *J. Asian Earth Sci.* **2015**, *97*, 320–336. [CrossRef]
128. Wang, T.; Jahn, B.-m.; Kovach, V.P.; Tong, Y.; Wilde, S.A.; Hong, D.-w.; Li, S.; Salnikova, E.B. Mesozoic intraplate granitic magmatism in the Altai accretionary orogen, NW China: Implications for the orogenic architecture and crustal growth. *Am. J. Sci.* **2014**, *314*, 1. [CrossRef]
129. Wang, Y.; Xue, C.; Wang, J.; Peng, R.; Yang, J.; Zhang, F.; Zhao, Z.; Zhao, Y. Petrogenesis of magmatism in the Yandong region of Eastern Tianshan, Xinjiang: Geochemical, geochronological, and Hf isotope constraints. *Int. Geol. Rev.* **2015**, *57*, 1130–1151. [CrossRef]
130. Wang, Y.; Zhao, C.; Zhang, F.; Liu, J.; Wang, J.; Peng, R.; Liu, B. SIMS zircon U–Pb and molybdenite Re–Os geochronology, Hf isotope, and whole-rock geochemistry of the Wunugetushan porphyry Cu–Mo deposit and granitoids in NE China and their geological significance. *Gondwana Res.* **2015**, *28*, 1228–1245. [CrossRef]
131. Wang, Y.-H.; Xue, C.-J.; Liu, J.-J.; Wang, J.-P.; Yang, J.-T.; Zhang, F.-F.; Zhao, Z.-N.; Zhao, Y.-J.; Liu, B. Early Carboniferous adakitic rocks in the area of the Tuwu deposit, eastern Tianshan, NW China: Slab melting and implications for porphyry copper mineralization. *J. Asian Earth Sci.* **2015**, *103*, 332–349. [CrossRef]
132. Zhang, C.; Zhang, X.; Santosh, M.; Liu, D.-D.; Ma, C.; Zeng, J.-H.; Jiang, S.; Luo, Q.; Kong, X.-Y.; Liu, L.-F. Zircon Hf-O-Li isotopes of granitoids from the Central Asian Orogenic Belt: Implications for supercontinent evolution. *Gondwana Res.* **2020**, *83*, 132–140. [CrossRef]
133. Zhang, F.; Wang, Y.; Liu, J.; Wang, J. Zircon U–Pb and molybdenite Re–Os geochronology, Hf isotope analyses, and whole-rock geochemistry of the Donggebi Mo deposit, eastern Tianshan, Northwest China, and their geological significance. *Int. Geol. Rev.* **2015**, *57*, 446–462. [CrossRef]
134. Zhang, F.-F.; Wang, Y.-H.; Liu, J.-J. Petrogenesis of Late Carboniferous granitoids in the Chihu area of Eastern Tianshan, Northwest China, and tectonic implications: Geochronological, geochemical, and zircon Hf–O isotopic constraints. *Int. Geol. Rev.* **2016**, *58*, 949–966. [CrossRef]
135. Zhang, X.; Yuan, L.; Xue, F.; Yan, X.; Mao, Q. Early Permian A-type granites from central Inner Mongolia, North China: Magmatic tracer of post-collisional tectonics and oceanic crustal recycling. *Gondwana Res.* **2015**, *28*, 311–327. [CrossRef]
136. Zheng, R.; Li, J.; Zhang, J. Juvenile hafnium isotopic compositions recording a late Carboniferous–Early Triassic retreating subduction in the southern Central Asian Orogenic Belt: A case study from the southern Alxa. *GSA Bull.* **2021**, *134*, 1375–1396. [CrossRef]
137. Kurapov, M.; Ershova, V.; Khudoley, A.; Luchitskaya, M.; Stockli, D.; Makariev, A.; Makarieva, E.; Vishnevskaya, I. Latest Permian–Triassic magmatism of the Taimyr Peninsula: New evidence for a connection to the Siberian Traps large igneous province. *Geosphere* **2021**, *17*, 2062–2077. [CrossRef]
138. Vernikovsky, V.A.; Pease, V.L.; Vernikovskaya, A.E.; Romanov, A.P.; Gee, D.G.; Travin, A.V. First report of early Triassic A-type granite and syenite intrusions from Taimyr: Product of the northern Eurasian superplume? *Lithos* **2003**, *66*, 23–36. [CrossRef]
139. Roy, K. Bjorne Formation (Lower Triassic), western Ellesmere Island. In *Report of Activities*; Geological Survey of Canada Paper; Geological Survey of Canada: Ottawa, ON, Canada, 1972; Volume 72-1, pp. 224–226.
140. Embry, A.F. Triassic history of the Tanquary High in NE Sverdrup Basin, Canadian Arctic Archipelago. *Geol. Soc. Am. Spec. Pap.* **2018**, *541*, 285–301.
141. Maurel, L. Geometry and evolution of the Tanquary structural high and its effects on the paleogeography of the Sverdrup basin, northern Ellesmere Island, Canadian Arctic. In *Current Research, Part G, Frontier Geoscience Program, Arctic Canada*; Geological Survey of Canada Paper; Geological Survey of Canada: Ottawa, ON, Canada, 1989; Volume 89-1G, pp. 177–189.
142. Beauchamp, B. Permian climatic cooling in the Canadian Arctic. *Geol. Soc. Am. Spec. Pap.* **1994**, *288*, 229–246.
143. Beauchamp, B.; Baud, A. Growth and demise of Permian biogenic chert along northwest Pangea: Evidence for end-Permian collapse of thermohaline circulation. *Palaeogeogr. Palaeoclimatol. Palaeoecol.* **2002**, *184*, 37–63. [CrossRef]
144. Beauchamp, B.; Alonso-Torres, D.; Piepjohn, K.; Thériault, P.; Grasby, S.E. Early Carboniferous syn-rift sedimentation in the Sverdrup Basin (Yelverton Pass area, northern Ellesmere Island, Arctic Canada): A solution to the Okse Bay problem. *Geol. Soc. Am. Spec. Pap.* **2018**, *541*, 255–284.
145. Amato, J.M.; Aleinikoff, J.N.; Akinin, V.V.; McClelland, W.C.; Toro, J. Age, chemistry, and correlations of Neoproterozoic–Devonian igneous rocks of the Arctic Alaska–Chukotka terrane: An overview with new U-Pb ages. *Geol. Soc. Am. Spec. Pap.* **2014**, *506*, 29–57.
146. Amato, J.M.; Toro, J.; Miller, E.L.; Gehrels, G.E.; Farmer, G.L.; Gottlieb, E.S.; Till, A.B. Late Proterozoic–Paleozoic evolution of the Arctic Alaska–Chukotka terrane based on U-Pb igneous and detrital zircon ages: Implications for Neoproterozoic paleogeographic reconstructions. *GSA Bull.* **2009**, *121*, 1219–1235. [CrossRef]
147. Gilmullina, A.; Klausen, T.G.; Paterson, N.W.; Suslova, A.; Eide, C.H. Regional correlation and seismic stratigraphy of Triassic Strata in the Greater Barents Sea: Implications for sediment transport in Arctic basins. *Basin Res.* **2020**, *33*, 1546–1579. [CrossRef]
148. Vermeesch, P.; Resentini, A.; Garzanti, E. An R package for statistical provenance analysis. *Sediment. Geol.* **2016**, *336*, 14–25. [CrossRef]
149. Müller, R.D.; Cannon, J.; Qin, X.; Watson, R.J.; Gurnis, M.; Williams, S.; Pfaffelmoser, T.; Seton, M.; Russell, S.H.J.; Zahirovic, S. GPlates: Building a Virtual Earth Through Deep Time. *Geochem. Geophys. Geosyst.* **2018**, *19*, 2243–2261. [CrossRef]

150. Cao, W.; Zahirovic, S.; Flament, N.; Williams, S.; Golonka, J.; Müller, R.D. Improving global paleogeography since the late Paleozoic using paleobiology. *Biogeosciences* **2017**, *14*, 5425–5439. [CrossRef]
151. Kos'ko, M.; Korago, E. Review of geology of the New Siberian Islands between the Laptev and the East Siberian Seas, North East Russia. *Stephan Mueller Spec. Publ. Ser.* **2009**, *4*, 45–64. [CrossRef]
152. Tuchkova, M.I.; Shokalsky, S.P.; Petrov, O.V.; Sokolov, S.D.; Sergeev, S.A.; Moiseev, A.V. Triassic deposits of Chukotka, Wrangel Island and Mendeleev Rise, Arctic Sea: Sedimentology and geodynamic implications. *GFF* **2020**, *142*, 158–168. [CrossRef]
153. Pózer Bue, E.; Andresen, A. Constraining depositional models in the Barents Sea region using detrital zircon U–Pb data from Mesozoic sediments in Svalbard. *Geol. Soc. Spec. Publ.* **2014**, *386*, 261–279. [CrossRef]
154. Klausen, T.G.; Rismyhr, B.; Müller, R.; Olaussen, S. Changing provenance and stratigraphic signatures across the Triassic–Jurassic boundary in eastern Spitsbergen and the subsurface Barents Sea. *Norw. J. Geol.* **2022**, *102*, 202205. [CrossRef]
155. Fleming, E.J.; Flowerdew, M.J.; Smyth, H.R.; Scott, R.A.; Morton, A.C.; Omma, J.E.; Frei, D.; Whitehouse, M.J. Provenance of Triassic sandstones on the southwest Barents Shelf and the implication for sediment dispersal patterns in northwest Pangaea. *Mar. Pet. Geol.* **2016**, *78*, 516–535. [CrossRef]
156. Flowerdew, M.J.; Fleming, E.J.; Morton, A.C.; Frei, D.; Chew, D.M.; Daly, J.S. Assessing mineral fertility and bias in sedimentary provenance studies: Examples from the Barents Shelf. *Geol. Soc. Spec. Publ.* **2020**, *484*, 255–274. [CrossRef]
157. Line, L.H.; Müller, R.; Klausen, T.G.; Jahren, J.; Hellevang, H. Distinct petrographic responses to basin reorganization across the Triassic–Jurassic boundary in the southwestern Barents Sea. *Basin Res.* **2020**, *32*, 1463–1484. [CrossRef]
158. Klausen, T.G.; Müller, R.; Slama, J.; Helland-Hansen, W. Evidence for Late Triassic provenance areas and Early Jurassic sediment supply turnover in the Barents Sea Basin of northern Pangea. *Lithosphere* **2017**, *9*, 14–28. [CrossRef]
159. Soloviev, A.V.; Zaionchek, A.V.; Suprunenko, O.I.; Brekke, H.; Faleide, J.I.; Rozhkova, D.V.; Khisamutdinova, A.I.; Stolbov, N.M.; Hourigan, J.K. Evolution of the provenances of Triassic rocks in Franz Josef Land: U/Pb LA-ICP-MS dating of the detrital zircon from Well Severnaya. *Lithol. Mineral Resour.* **2015**, *50*, 102–116. [CrossRef]
160. Amato, J.M.; Toro, J.; Akinin, V.V.; Hampton, B.A.; Salnikov, A.S.; Tuchkova, M.I. Tectonic evolution of the Mesozoic South Anyui suture zone, eastern Russia: A critical component of paleogeographic reconstructions of the Arctic region. *Geosphere* **2015**, *11*, 1530–1564. [CrossRef]
161. Dumoulin, J.A.; Whidden, K.J.; Rouse, W.A.; Lease, R.O.; Boehlke, A.; O'Sullivan, P. Biosiliceous, organic-rich, and phosphatic facies of Triassic strata of northwest Alaska: Transect across a high-latitude, low-angle continental margin. *Geol. Soc. Am. Spec. Pap.* **2022**, *556*, 243–271.
162. Amato, J.M.; Dumoulin, J.A.; Gottlieb, E.S.; Moore, T.E. Detrital zircon ages from upper Paleozoic–Triassic clastic strata on St. Lawrence Island, Alaska: An enigmatic component of the Arctic Alaska–Chukotka microplate. *Geosphere* **2022**, *18*, 1492–1523. [CrossRef]
163. Vermeesch, P. Maximum depositional age estimation revisited. *GSF* **2021**, *12*, 843–850. [CrossRef]
164. Vernikovsky, V.; Vernikovskaya, A.; Proskurnin, V.; Matushkin, N.; Proskurnina, M.; Kadilnikov, P.; Larionov, A.; Travin, A. Late Paleozoic–Early Mesozoic Granite Magmatism on the Arctic Margin of the Siberian Craton during the Kara-Siberia Oblique Collision and Plume Events. *Minerals* **2020**, *10*, 571. [CrossRef]
165. Steel, R.J.; Worsley, D. Svalbard's post-Caledonian strata—An atlas of sedimentational patterns and palaeogeographic evolution. In Proceedings of the Petroleum Geology of the North European Margin, Trondheim, Norway, 9–11 May 1983; Springer: Dordrecht, The Netherlands, 1984; pp. 109–135.
166. Lord, G.S.; Johansen, S.K.; Støen, S.J.; Mørk, A. Facies development of the Upper Triassic succession on Barentsøya, Wilhelmøya and NE Spitsbergen, Svalbard. *Norw. J. Geol.* **2017**, *97*, 33–62. [CrossRef]
167. Klausen, T.G.; Mørk, A. The Upper Triassic paralic deposits of the De Geerdalen Formation on Hopen: Outcrop analog to the subsurface Snadd Formation in the Barents Sea. *AAPG Bull.* **2014**, *98*, 1911–1941. [CrossRef]
168. Glørstad-Clark, E.; Faleide, J.I.; Lundschien, B.A.; Nystuen, J.P. Triassic seismic sequence stratigraphy and paleogeography of the western Barents Sea area. *Mar. Pet. Geol.* **2010**, *27*, 1448–1475. [CrossRef]
169. Klausen, T.G.; Ryseth, A.E.; Helland-Hansen, W.; Gawthorpe, R.; Laursen, I. Regional development and sequence stratigraphy of the Middle to Late Triassic Snadd Formation, Norwegian Barents Sea. *Mar. Pet. Geol.* **2015**, *62*, 102–122. [CrossRef]
170. Riis, F.; Lundschien, B.A.; Høy, T.; Mørk, A.; Mørk, M.B.E. Evolution of the Triassic shelf in the northern Barents Sea region. *Polar Res.* **2008**, *27*, 318–338. [CrossRef]
171. Gilmullina, A.; Klausen, T.G.; Doré, A.G.; Sirevaag, H.; Suslova, A.; Eide, C.H. Arctic sediment routing during the Triassic—Sinking the Arctic Atlantis. *J. Geol. Soc.* **2022**, *180*, jgs2022-018. [CrossRef]
172. Embry, A.F. The Heiberg Group, western Sverdrup Basin, Arctic Islands. In *Current Research, Part B*; Geological Survey of Canada Paper; Geological Survey of Canada: Ottawa, ON, Canada, 1983; Volume 83-1B, pp. 381–389.
173. Boekhout, F.; Roberts, N.M.W.; Gerdes, A.; Schaltegger, U. A Hf-isotope perspective on continent formation in the south Peruvian Andes. *Geol. Soc. Spec. Publ.* **2015**, *389*, 305–321. [CrossRef]
174. Kohanpour, F.; Kirkland, C.L.; Gorczyk, W.; Occhipinti, S.; Lindsay, M.D.; Mole, D.; Le Vaillant, M. Hf isotopic fingerprinting of geodynamic settings: Integrating isotopes and numerical models. *Gondwana Res.* **2019**, *73*, 190–199. [CrossRef]
175. Spencer, C.J.; Kirkland, C.L.; Prave, A.R.; Strachan, R.A.; Pease, V. Crustal reworking and orogenic styles inferred from zircon Hf isotopes: Proterozoic examples from the North Atlantic region. *GSF* **2019**, *10*, 417–424. [CrossRef]
176. Puchkov, V.N. Structural stages and evolution of the Urals. *Mineral. Petrol.* **2013**, *107*, 3–37. [CrossRef]

177. Ledneva, G.V.; Pease, V.L.; Sokolov, S.D. Permo-Triassic hypabyssal mafic intrusions and associated tholeiitic basalts of the Kolyuchinskaya Bay, Chukotka (NE Russia): Links to the Siberian LIP. *J. Asian Earth Sci.* **2011**, *40*, 737–745. [CrossRef]
178. Sokolov, S.D.; Ledneva, G.V.; Pease, V.L. New data on the age and genesis of igneous rocks in the Kolyuchinskaya Guba (eastern Chukotka). *Dokl. Earth Sci.* **2009**, *425*, 384–388. [CrossRef]
179. Kuzmichev, A.B.; Pease, V.L. Siberian trap magmatism on the New Siberian Islands: Constraints for Arctic Mesozoic plate tectonic reconstructions. *J. Geol. Soc.* **2007**, *164*, 959. [CrossRef]
180. Sømme, T.O.; Doré, A.G.; Lundin, E.R.; Tørudbakken, B.O. Triassic–Paleogene paleogeography of the Arctic: Implications for sediment routing and basin fill. *AAPG Bull.* **2018**, *102*, 2481–2517. [CrossRef]
181. Harrison, J.C.; Brent, T.A. Basins and fold belts of Prince Patrick Island and adjacent areas, Canadian Arctic Islands. *Geol. Surv. Can. Bull.* **2005**, *560*, 208.
182. Miall, A.D. Mesozoic and Tertiary geology of Banks Island, Arctic Canada: The history of an unstable craton margin. *Geol. Surv. Can. Mem.* **1979**, *387*, 1–235.
183. Müller, R.; Klausen, T.G.; Faleide, J.I.; Olaussen, S.; Eide, C.H.; Suslova, A. Linking regional unconformities in the Barents Sea to compression-induced forebulge uplift at the Triassic-Jurassic transition. *Tectonophysics* **2019**, *765*, 35–51. [CrossRef]